



OPEN Multifaceted enhancement of piezoelectricity and optical fluorescence in electrospun PVDF-ceria nanocomposite

Nader Shehata^{1,2,3,4}, Remya Nair^{1,5}, Ankur Jain⁶, Mohammed Gamal², Ahmad Hassanin^{2,7,8}, Sara Noman^{2,9}, Islam Shyha¹⁰, Krzysztof Kruczała¹¹, Marwa Saad¹¹✉ & Ishac Kandas^{2,3}

This study investigates the enhancement of piezoelectric and optical fluorescence properties in electrospun polyvinylidene fluoride (PVDF) nanocomposite membranes doped with cerium oxide (Ce³⁺) at varying weight percentages. An optical characterisation using absorbance analysis found a blue shift in the bandgap of the ceria NPs, which also enhanced UV absorption in the PVDF polymer. At some additive doses, luminosity analysis demonstrated an incremental fluorescence impact. However, above a certain point, additional increases seemed to have a quenching effect, which decreased fluorescence. FTIR based analysis revealed the enhanced β sheets content to 61.75% in the sample of PVDF with a ceria 5 wt%. The fabricated nanofiber membrane displayed an average fiber diameter of around 108 nm. XRD analysis confirms that the incorporation of Ce³⁺ significantly promotes the formation of the β -phase in PVDF, thereby improving its piezoelectric response. Additionally, water contact angle measurements indicate increased hydrophobicity in the nanocomposite membranes, expanding their applicability in sensing and energy harvesting applications. ICP-OES and XRF analysis confirm that Ce was successfully incorporated with the PVDF chain. The dual role of ceria as both a nucleating agent for β -phase formation and an optical fluorescence enhancer highlights its potential for the development of multifunctional nanocomposites. This work presents a novel approach to engineering PVDF-based materials with enhanced piezoelectricity and optical fluorescence for advanced technological applications. This ultrasensitive PVDF with a ceria 5 wt% nanogenerator demonstrated pronounced piezoactivity, generating a maximum of 9 V with 3 N load at 1.5 Hz frequency which is almost three times of the output generated by pure PVDF. The formed oxygen vacancies according to tri-valent cerium ions, which have been showed through optical characteristics, supports the nucleation of PVDF chains around ceria NPs. The resultant PVDF/ceria nanomembrane demonstrated a remarkable maximum power density of 89 mW/m², demonstrating its load-bearing capability. With its dual functionality as an optical sensor and an energy harvesting unit, this adaptable nanocomposite shows potential for use in multifunctional devices.

Keywords Fluorescent nanostructure, Beta phase, Percolation threshold, Absorbance, Electroactive phase, Crystallinity

Piezoelectric nanostructures are a special class of smart materials that possess the ability to harness electrical energy from mechanical vibrations and the principle of piezoelectricity can be utilized for energy harvesting

¹Kuwait College of Science and Technology, Doha Area, 7th Ring Road, 13133 Safat, Kuwait. ²Centre of Smart Materials, Nanotechnology and Photonics (CSNMP), Smart CI Research Centre, Alexandria University, Alexandria 21544, Egypt. ³Department of Engineering Mathematics and Physics, Faculty of Engineering, Alexandria University, Alexandria 21544, Egypt. ⁴School of Engineering, Ulster University, Belfast BT15 1AP, Northern Ireland, UK. ⁵School of Applied Sciences, Suresh Gyan Vihar University, Jaipur, India. ⁶Centre for Renewable Energy & Storage, School of Applied Sciences, Suresh Gyan Vihar, University, Jaipur, India. ⁷Department of Textile Engineering, Faculty of Engineering, Alexandria University, Alexandria 21544, Egypt. ⁸Wilson College of Textiles, NC State University, Raleigh, NC, USA. ⁹Physics department, Faculty of Science, Mansoura University, Mansoura 35516, Egypt. ¹⁰School of Computing Engineering and the Built Environment, Edinburgh Napier University, Edinburgh, UK. ¹¹Faculty of Chemistry, Jagiellonian University in Krakow, Gronostajowa 2, 30-387 Kraków, Poland. ✉email: marwa.saad@uj.edu.pl

applications where the unused vibrations, mechanical motions or human body generated movements can be employed for reaping electrical energy for low power devices. Ambient energy based harnessing mainly requires flexibility and adaptability nature and thereby our field of focus is on polymer based nanogenerators where the incorporation of some organic/inorganic additives, even some ceramics or crystals can enhance the piezoactivity^{1–5}. This work focuses on the crystalline piezoelectric material PVDF, produced through free radical polymerization of 1,1-difluoroethylene ($\text{CH}_2=\text{CF}_2$). PVDF has exceptional electroactive characteristics, flexibility, stability, weightlessness, and excellent mechanical, thermal, and biocompatible qualities. Its polymorphic structure is due to inter-structural transformation and molecular chain packing, with the crystalline behavior mainly responsible for the net dipole moment of the polymer chain^{6–8}. The chain configuration of PVDF is shown in Fig. 1.

Among the five polymorphic phases, α , β , and γ are commonly available crystalline phases out of which β phase is the most important one due to its piezoelectric property. The β phase in PVDF nanofibers exhibits significant piezoelectric properties due to the alignment of dipole moments in parallel orientation, where C–F dipoles and C–C chain backbone are arranged in such a way that they cancel each other as shown in Fig. 1b. Enhancing piezoelectric property in general requires optimization of factors such as crystallinity, β phase content, dipole alignment, and molecular chain alignment^{9–13}. The α phase, the most common phase, can be converted into its polar forms and then finally in to β phase by the application of high electric fields and simple poling techniques¹⁴.

Electrospinning is a specific electrohydrodynamic fabrication process driven by a high voltage for the production of ultrafine nanofibers and present study utilizes this fabrication technique for the production of beta phase rich nanofibers. It stands out as the most convenient and efficient method for generating long, flexible nanofibers with controlled diameters (from 50 to 1000 nm) and morphology, offering easy orientation direction for various applications^{15–22}. Incorporating nanofillers with PVDF improves β phase content but can cause induced charges at the boundary, affecting crystallinity. The effect of nanoparticles only works positively above a percolation threshold, which is the specific concentration of nanoparticle content above which the rheological properties increase exponentially. These NPs act as nucleate agents in the initial crystallization process, supplying energy for alpha-to-beta phase transformation. Also, electrically conductive nanofillers can improve the alignment of dipoles during poling process. Active nanofillers improve the properties and piezoresponse of pure nanofibers, enabling multipurpose applications. For instance, gold nanoparticles (Ag NPs)– and carbon dots based PVDF electrospun nanofibers show enhanced piezoresponse and acoustic sensing. Silver nanoparticles (Au NPs) incorporated PVDF nanofibers show improved crystal area and electrothermal effects, making them suitable for tissue engineering scaffolds^{23–25}. Moreover, the addition of ZnO, HFP, TBAC, CD, PZT, and Cu NPs significantly boosted the PVDF-based nanostructures' piezoactivity^{16,26–30}. Fluorescent nanostructures are additives that enhance the optical activity or behaviour of nanofibers in polymer solutions. Photoluminescent electrospun nanofibers, fabricated by incorporating inorganic precursor materials, are crucial in optical nanosensors due to their fluorescence quenching mechanism. NaYF₄: Eu + 3 nanophosphor is an important additive for a range of polymers as part of luminescent composite nanofiber fabrication, suitable for lighting applications, which is based on fluorescence quenching mechanism^{31–37}. Ceria has been found to be a propitious optically active nanoparticle having effective oxide storage capacity based on reduction–oxidation (redox) features. The oxygen vacancies that occur within the crystalline framework of cerium serve as adsorbing sites for charged small metal-based particles, oxygen, and radicals. The production of tri-valent cerium ions trap energy levels, which are optically active due to a lowered bandgap near 3 eV, is linked to those vacancies³⁸. Ceria has been found to be effective in incorporating chitosan nanofibers thus the incorporation of ceria like NPs onto a piezoelectric polymer solution like PVDF can generate optical activity³⁸. In addition, the piezo-enhancement property of ceria NPs while incorporated onto polymer like PVDF is proved from some literatures³⁹. The addition of inorganic NPs like ceria can modify polymer properties and generate electroactive phases such as β and γ ⁴⁰. The electroactive phase generation is due to the ion dipole interaction by the incorporation of surface charged NPs⁴¹. Ceria nanostructures are efficient fluorescent nanostructures with excellent thermal stability, dielectric properties, high surface area, large pore volume, and ionic conductivity^{42–44}. Cerium, a rare earth lanthanide element with low toxicity, has oxygen storage capacity and reduction–oxidation processes, making them important in fluorescence and optical activity applications. Under ultraviolet excitation, ceria produces visible

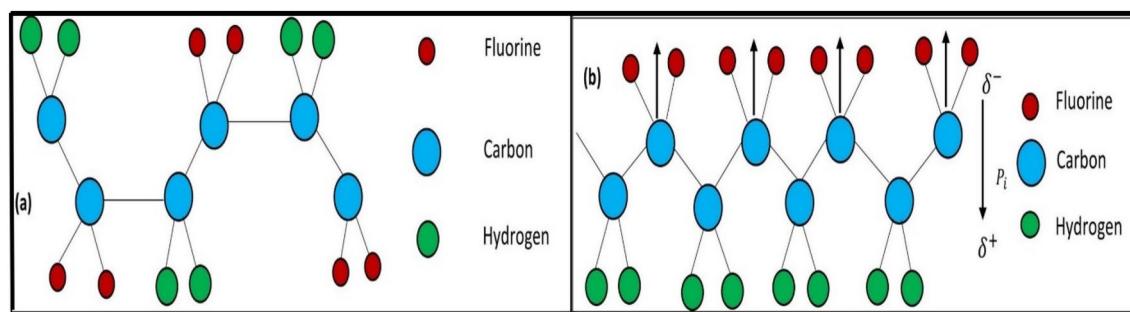


Fig. 1. (a) Chain configurations of PVDF, and (b) PVDF crystalline piezoelectric β (TTTT) phase showing resultant nonzero dipole moment.

fluorescence emission, leaving oxygen vacancies for quenchers^{45,46}. Cerium nanostructures has dual ionization states; Ce^{3+} and Ce^{4+} and among these two states, cerium trivalent trap state is responsible for the fluorescent or optical properties where the transition occurs from 5d–4f energy levels. The fluorescence lifetime is associated with the time taken by the trivalent cerium ion in the excitation state^{38,47}. The scope of the incorporation of ceria nanoparticles within polymers are reported in several recent works including biomedical application. The potential uses of cerium nanoparticles (CeO_2 NPs) in anti-oxidation, cancer treatment, photocatalytic pollution degradation, sensors especially as optical sensors for water quality monitoring and other areas have made them desirable materials in both the biomedical and industrial domains^{48–53}.

The above previous studies have primarily focused on enhancing the β -phase content in PVDF using various metal oxides without considering additional functionalities such as optical fluorescence. Ceria (Ce^{3+})-doped PVDF has not been extensively studied, particularly in terms of its dual role in enhancing both piezoelectric and optical properties. While previous reports suggest that rare-earth dopants can improve certain dielectric characteristics of PVDF, their nucleating effects on β -phase formation and fluorescence enhancement remain largely unexplored. This study addresses this gap by systematically investigating the role of Ce^{3+} in tuning PVDF's structural, electrical, and optical properties. Our findings demonstrate that Ce^{3+} acts as a nucleating agent, increasing the β -phase fraction and consequently improving the piezoelectric response. Additionally, Ce^{3+} imparts fluorescence properties, making the nanocomposite multifunctional. These dual enhancements make PVDF-ceria nanocomposites promising candidates for applications in flexible sensors, energy harvesters, and bioelectronics. In the present study, we used ceria NPs as nanofillers, where the piezoelectric properties of PVDF can be controlled by their addition. Based on the understanding from literatures, our aim is to focus on the scope of PVDF ceria-based nanofibers in the field of multifunctional sensors by including the best optimum content of ceria NPs that can be incorporated successfully without affecting the morphology of pure PVDF nanofibers. Cerium nanoparticles are prepared using the chemical precipitation technique. Finally, the prepared NPs are added on to the PVDF solution based on the required concentration and the mixture solution is loaded for electrospinning process where PVDF/ceria nanofibers will be fabricated. The multifunctional behaviour such as piezo enhancement and optical activity of these nanocomposite-based nanofibers is analysed. Piezoactivity based application mainly includes the field of sensors and energy harvesting, while optical activity paves a way in the field of UV filters and environmental pollutant sensing⁵⁴. Thus, our aim is to develop a highly efficient optically active piezoelectric fluorescent nanofibers that has a multifunctional behaviour⁵⁵. This new inorganic–organic nanofiber greatly improves scope of PVDF nanofiber as a multifunction piezoelectric/fluorescent nanocomposite mat that can be helpful in the applications of solid-state lighting and vibration sensing.

Experimental work

Materials

The materials included in this study consist of polymer–Poly vinylidene difluoride (PVDF) purchased from Sigma Aldrich and (Kynar[®], King of Prussia, PA, USA) supplied by ARKEMA, Dimethyl Formamide (DMF) (DMF 98%, Sigma Aldrich, Taufkirchen, Germany as solvent, Cerium (III) chloride heptahydrate (Sigma Aldrich, St. Louis, MO, USA), distilled water, and ammonium hydroxide. By using a rotary viscometer (DVII+, Brookfield, USA) at room temperature, the viscosity of the solution is measured and found is to be 810 cps.

Nanocomposite developing and manufacturing

Ceria nanoparticle and polymer solution preparation

Ceria in the present study is prepared by using chemical precipitation technique and the block diagram with detailed preparation procedure is provided in the supplementary file in Figure S1. It is a straightforward procedure and the chemical precursors are cost effective. In addition, the chemical precipitation technique promotes the growth of pronounced Ce^{3+} ions, while comparing with other preparation techniques⁵⁶. The polymeric solution of PVDF is prepared by adding 1 gm of PVDF to 10 mL of Dimethylformamide and the solution is left on magnetic stirrer at room temperature for continuous stirring for approximately 20 h such that a clear homogenous solution is obtained. Finally, PVDF solution is mixed with different weight percentage of ceria NPs based on the requirement and the whole solution is stirred for around 24 h so that a homogeneous solution is obtained. During the 24-h mixing period, the nanoparticles have adequate time to grow and crystallize, especially when the process is conducted in an environment like DMF. Longer mixing times may allow for the formation of larger and more crystalline CeO_2 particles. DMF promotes the solubility of the cerium precursor, which aids in the nucleation and crystallization of CeO_2 nanoparticles.

The selected weight percent of ceria NPs are in the range from 0.5 to 6%. The concentration of cerium precursor plays a role in the crystallization process. Higher concentrations of Ce can lead to a higher number of nucleation sites, potentially resulting in smaller nanoparticles if the mixing time and other parameters are not optimized. However, if the mixing time is sufficiently long, the increased concentration of Ce could lead to larger or more crystalline CeO_2 nanoparticles, as the excess cerium ions have enough time to properly incorporate into the crystalline structure. Each time the blended solution is loaded onto the syringe for electrospinning process. Subsequently, each blended solution is loaded onto the syringe for the electrospinning process. The most common methods for synthesizing CeO_2 nanoparticles are sol–gel, hydrothermal, and combustion method. The sol gel method has been frequently used for producing CeO_2 nanoparticles due to its ability to control particle size and morphology. In a typical sol–gel approach, cerium nitrate ($Ce(NO_3)_3 \cdot 6H_2O$) is used as the cerium precursor, and PVDF can be coated by dissolving both the precursor and PVDF in an organic solvent. A study by Chakraborty et al.⁵⁷ demonstrated the synthesis of CeO_2 -PVDF nanocomposites via sol–gel, where cerium precursors were dispersed in the polymer matrix, resulting in nanoparticles uniformly distributed on PVDF. The crystalline quality of CeO_2 nanoparticles enhance using a hydrothermal process⁵⁸. Chemical vapor deposition (CVD) can also be used to deposit CeO_2 films on PVDF by reacting cerium-containing gases in a heated chamber preferred

when highly uniform coatings are required⁵⁹. However, direct mixing of CeO₂ nanoparticles with PVDF in a solvent followed electrospinning is also explored for fabricating nanocomposites with enhanced mechanical or electrochemical properties. The mechanisms behind these methods include physical interactions such as van der Waals forces, electrostatic interactions, and enhance chemical bonding between the inorganic and organic phases^{18,60}.

Electrospinning process

The inorganic polymeric nanocomposite structure in the form of nanofibers can be fabricated using electrospinning technique and the setup with explanation is shown in supplementary file as Figure S2. The electrospinning process involves the orientation of C–F dipoles along the electric field, resulting in tighter packing density of β phase with all Trans conformation. Above 5% concentration, ceria NPs started behaving negatively even affecting electrospinning, leading to electrospaying-like behaviour that altered the shape of the nanofibers. Even agglomeration inside the syringe needle is observed above 5 wt% and this prevented fiber formation. As a result, the process of creating nanofibers by incorporating NPs was halted at the 5 wt% threshold and thoroughly examined to verify their effectiveness.

Piezoelectric characterization of the PVDF/ceria nanofibers membrane

The piezoelectric voltage generated by the nanofibers mat for different compressive loads/forces at different applied frequencies is performed using a custom-made setup as shown in supplementary file Figure S4. A spring motor-based arrangement is used to apply cyclic forces, where the applied compressive loads are exerted vertically onto the nanofibers patches using a pressing head of 1 cm diameter. The compressive loads were applied in the range from 0.5 to 3 N in steps of 0.5 N for different frequencies such as 0.5 Hz, 1 Hz, and 1.5 Hz.

Results and discussion

Optical properties of the nanofibers composite

The UV–Vis spectrophotometer (SHIMADZU UV-2600) was employed to measure the optical absorbance of ceria NPs and the ceria integrated PVDF nanofibers. Optical characterization involved assessing absorbance, fluorescence intensity, and direct band gap measurements. For absorbance and direct band gap calculation, we used UV Vis spectrophotometer-based measurements, and another separate experimental setup is used for fluorescence study and the detailed explanation about experimental setup is shown in the supplementary file as Figure S3. The addition of optically active inorganic materials onto the PVDF polymer which is an organic material enhances the stability and processability of the composite with some interesting optical properties. Polymer based composition can show an efficient tunability in their optical activity by regulating the concentration of the dopants used. Here we used optically active ceria NPs as inorganic dopants onto the organic PVDF polymer where ceria NPs are dispersed on to the polymer matrix. A very small fraction of NPs in the range 1–5% is used for the optical study and even this small fraction resulted in the improvement of the optical properties of the polymeric composite.

Bandgap calculation of the dopant used with PVDF is measured based on the optical characterisation such as absorbance where the light electron interaction is studied. The absorption edge of pure PVDF is around 202 nm which is clearly visible from its absorption spectrum, as shown in Fig. 2a. The semi-crystalline nature of PVDF is clearly represented by this sharp absorption edge. The absorption spectrum of pure PVDF shown a broad band covering 202 nm to around 270 nm with a central region of 255 nm. Thus, UV absorption window can be enhanced by the addition of some of the inorganic NPs such as ceria. The absorption spectrum of pure ceria NPs exhibited a broad band around 300 to 400 nm with peak around 340 nm which is visible in Fig. 2a. The absorption edges are found to be around 298 nm and 400 nm in the blue and red side, respectively. Thus, the absorption edge of PVDF/ceria nanocomposite membrane is found to be shifted to the longer wavelength side covering UV A (315–400 nm), UV B (280–315 nm) and a part of UV C (100–280 nm) region which clearly represents the use of these composites in the field of efficient UV filters as shown in Fig. 2a. The electrons are excited from valence band to conduction band using the photon energy and this is the main mechanism behind UV absorption. Thus, the incorporation of ceria dopant greatly enhanced the UV absorption of PVDF which clearly improved the scope of the composite in commercial applications. The optical absorption spectrum of pure ceria using UV–VIS spectrophotometer has shown a broadband around 300 to 400 nm. This broad absorption band corresponds to the charge transfer transition into the 4f band of Ce⁴⁺ in CeO₂ from 2p valence band of O²⁻. In general, for ceria the bandgap is formed between the valence band top portion of oxygen (O) (2P) states and conduction band bottom part formed by Ce (4f) states.

UV–Vis spectra pure PVDF and CeO₂ are different in width and position. However, UV–Vis spectrum of PVDF doped with Ce are overlapped. Therefore the 2nd derivative of PVDF and PVDF doped with 5 wt% of ceria as presented in Fig. 2 is used to differentiate between UV–Vis spectra and avoid overlapping. UV–Vis spectrum of the 2nd derivative shows a slightly red shift at 218 nm to 224 nm and another shift from 250 to 265 nm after doping PVDF with 5%Ce, proving the presence of interaction between Ce and the PVDF polymer chain. Also, Fig. 7 shows a clear hyperchromic effect that was observed in the UV–vis spectrum PVDF with 5% Ce. This indicates that the absorption property of PVDF changed by surface modification and crystallization. According to Fig. 2a, the absorbance peak of pure CeO₂ located at 340 nm but after introducing the Ce–O into the PVDF matrix the absorbance peak shifted to 265 nm (toward short wavelength -blue shift). Tsunekawa et al.⁵⁹ explained this shift by the transition of Ce⁴⁺ to Ce³⁺ ions.

The absorbance dispersion curves of the electrospun PVDF/ceria nanofibers embedded with different ceria concentrations are studied. The absorbance dispersion curves of the independent ceria NPs are also analyzed based on the model proposed by Tauc's relation. The absorbance dispersion curves are used to calculate the bandgap of the corresponding ceria NPs involved and the equation involved is represented as:

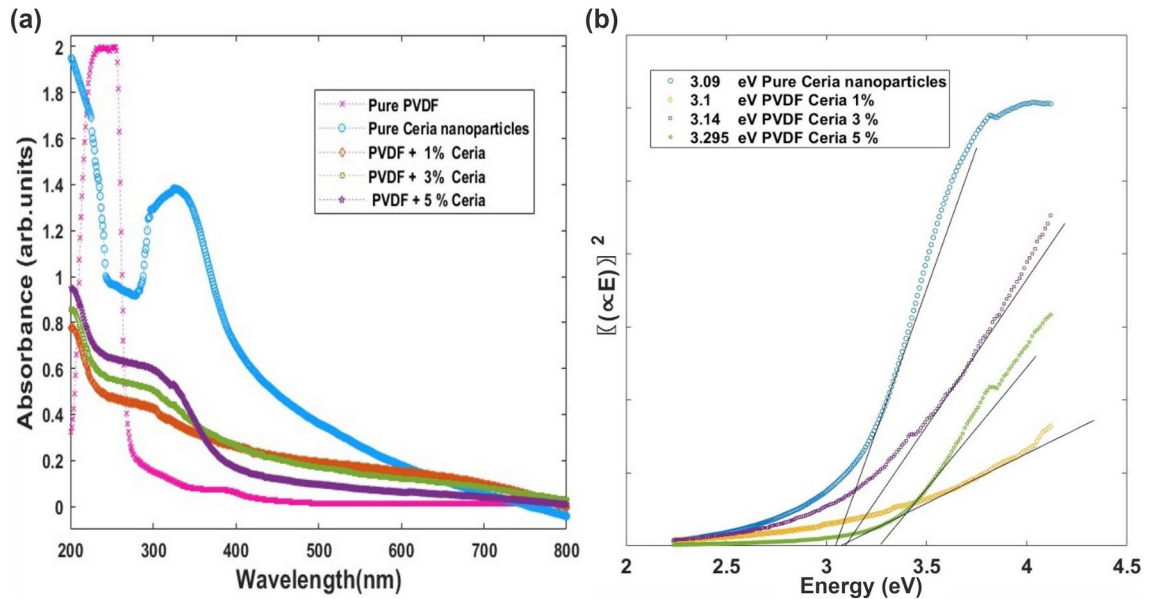


Fig. 2. (a) UV–VIS based absorption spectrum of Pure PVDF nanofibers, Pure ceria NPs and PVDF/ceria nanofibers of different ceria concentrations, (b) Direct bandgap of ceria NPs and PVDF/ceria nanocomposite nanofibers.

$$\alpha(E) = A(E - E_g)^{1/2} \quad (1)$$

where α represents the absorption coefficient that quantifies the rate of reduction in the intensity of electromagnetic radiation due to the passage of light through it, A is a constant associated with the material property based on the dielectric constant and effective mass of the electrons and holes, E represents the absorbed photon energy, and the allowed direct band gap is denoted as E_g for the produced nanocomposite^{56,61–63}. Based on Eq. 1, a plot of $[\alpha(E)]^2$ versus E is used to analyze the bandgap of the corresponding nanocomposite. The linear part of the plot is extrapolated to the x-axis and the intersection position of the extrapolation on the x-axis will be the actual bandgap of the involved material⁶¹. The power or exponent of $(E - E_g)^r$ in general is denoted as $(E - E_g)^r$, where ‘ r ’ represents the power factor of transition mode and can take values 1/2, 2, 3/2 and 3. Here ‘ $r = 1/2$ ’ represents allowed direct electronic transition and ‘2’ represents indirect electronic transition and so on. In the present case, from Eq. 1 it’s clear that the transition mode is represented by the value of ‘ $r = 1/2$ ’, representing direct allowed transition and thereby demonstrating allowed direct band gap. The absorbance curve of the pure ceria NPs and the PVDF/ceria nanofibers at different ceria concentrations are shown in Fig. 2 and the corresponding absorbance dispersion curve is shown in Fig. 2b. In Fig. 2b, the extrapolation of the linear part is clearly shown, and the intersection is biased within 3–3.5 eV region, which clearly indicates that the bandgap values are within the accepted range based on studies^{38,47,56}. This value of bandgap indicates the presence of trivalent Ce^{3+} ions which is associated with the number of oxygen vacancies inside the nanocomposite, and it establishes a trap state 3 eV over the CeO_2 valence band and it is associated with the $\text{Ce}^{5d} - \text{Ce}^{4f}$ transition. The bandgap value of ceria NPs is determined to be approximately 3.09 eV. Meanwhile, PVDF/ceria nanofibers with concentrations ranging from 1 to 5% exhibit bandgap values within the range of 3.1 to 3.31 eV. This substantiates the presence of Ce^{3+} ions, which are accountable for the observed optical activity⁶⁴. The blue shift in bandgap value is based on the reduction of particle size arising from the quantum effects due to the effective or higher localization of energy bands and finally the bands will be reduced to atomic states⁶⁵. For the composite nanofibers, a significant amount of ceria atoms is present on the external surface, and this results in the generation of oxygen vacancies and defects, and it greatly influences the bandgap⁶⁶.

In addition to the absorbance, a fluorescence emission curve around 520 nm is obtained for pure ceria NPs under an excitation of visible 430 nm wavelength and the fluorescence emission curve for different concentrations of the embedded ceria in situ in the electrospun PVDF nanomembrane is also analyzed and the corresponding plots are shown in the Fig. 3. The fluorescence emission peak in ceria is due to the trivalent Ce^{3+} ions via its relaxation from 5d–4f states. The fluorescence intensity peak height was found to be increasing for a concentration from 0.5–2 wt%. The fluorescence emission intensity is found to be the maximum for a concentration of 2% ceria and a further increase in concentration affected the emission intensity negatively showing a decrease in the peak height. The fluorescence plot clearly shows that the intensity is minimum for a concentration of 3 wt% and even an increase in concentration from 3–5 wt% resulted in a minor increase in the intensity, but still less than 2% concentration. The process of static fluorescence quenching, which results in the production of a nonfluorescent complex that lowers the emission intensity, can be used to explain the reduction in emission intensity for larger concentrations. The visible luminescence of the nanosized ceria particles in their pure state and along with PVDF as a dopant is generated from the oxygen vacancy related states⁴².

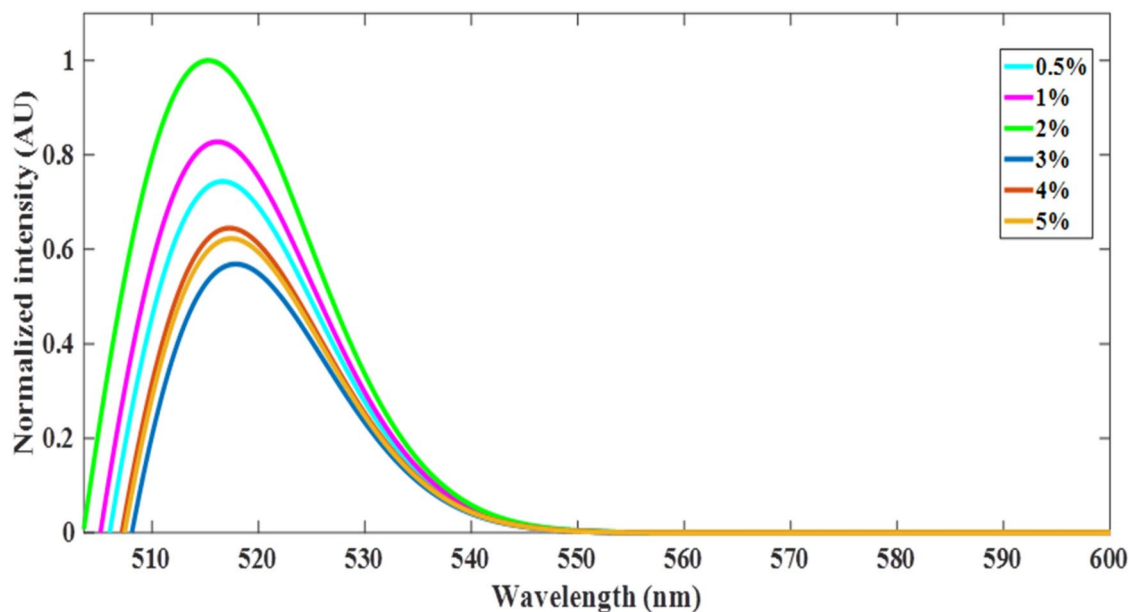


Fig. 3. Fluorescence spectra of PVDF/ceria nanofibers samples.

Morphological characterisation of the fabricated PVDF/ceria nanofibers using SEM

The surface characterization of the PVDF/ceria nanocomposite nanofibers is performed using Scanning Electron Microscope (SEM) (JEOL JSM-6010LV-SEM, Tokyo, Japan). The diameter and surface morphology of the composite nanofibers is analyzed in detail at an accelerating voltage of 20 kV using a sample size of 1×1 cm. ImageJ software is used to study the size distribution of the nanofibers imaged by the SEM. In addition, to measure the diameter of the NPs and confirm the presence of it, a transmission electron microscopy (TEM) (JEM-1400 PLUS, JEOL, Tokyo, Japan) was used. EDS mapping was performed using a (JEOL JSM-6010LV-SEM, Tokyo, Japan) SEM equipped with an EDS detector. The accelerating voltage was set to 20 kV, and the working distance was maintained at 100 μm . Elemental maps were obtained for carbon, fluorine, oxygen, and cerium to assess the distribution of ceria nanoparticles within the PVDF matrix.

Electrospun PVDF with ceria 5 wt% nanofibers membrane was studied under SEM. Figure 4a represents the corresponding SEM images of ceria embedded PVDF electrospun nanofibers in 1 μm scale. The images clearly depict the random distribution of nanofibers with ceria NPs sailing or floating across the network of nanofibers. The diameter of the randomly distributed nanofibers is measured using the ImageJ software and the corresponding fiber diameter distribution is shown in Fig. 4b. The average diameter of the generated nanofibers is measured to be around 108.002 nm. In the 5% PVDF/ceria nanocomposite, uniform distribution of ceria NPs is an essential component to be considered. The accumulation of NPs reduces the crystallinity and that results in crystal defects. However, uniform dispersion can largely enhance the overall crystallinity^{65,67}. Transmission Electron Microscope (TEM) based imaging is used to visualise the ceria NPs as shown in Fig. 4c and d.

The Energy Dispersive Spectroscopy mapping of PVDF/ceria 5% nanofibers shows the elemental composition and distribution of the electrospun PVDF/ceria 5% nanofibers. EDS mapping can provide spatially resolved chemical information, which is very important in realizing the uniformity of dispersion of ceria nanoparticles within nanofibers. As shown in Fig. 5, corresponding EDS elemental maps of PVDF/ceria nanofibers. The EDS maps represent local distributions of fluorine (red), carbon (brown), oxygen (blue), and cerium (turquoise), within the matrix of nanofibers.

The EDS maps have also shown that cerium is fairly dispersed in nanofibers, indicative of the fact that ceria nanoparticles disperse well inside the matrix of PVDF. Such uniformity in dispersion is important for maintaining consistent piezoelectric and mechanical properties throughout the material. Oxygen and fluorine mapping further confirmed the nature of the composition of the PVDF/ceria nanocomposite. The quantitative EDS disclosed that the ceria content in the nanofibers was about 5 wt%, which was expected according to the targeted loading during synthesis. Carbon and fluorine contents were also quantified in accordance with the expected composition of the PVDF matrix.

Crystallinity and phase identification for PVDF/ceria nanomembrane

The molecular fingerprint and the β phase content of the fabricated nanofibers is studied using FTIR spectrometer. Fourier transform infrared spectroscopy (FTIR) is an essential analysis tool for identifying the chemical structure of a material based on atomic vibrations of the molecules involved. The molecular structure mainly represents chemical bond and functional group based on characteristic frequencies. The FTIR spectra of the PVDF/ceria composition were generated using a Vertex 70 FTIR (Bruker, Billerica, MA, USA) at a scanning resolution of 5 cm^{-1} around a range of $4000\text{--}400 \text{ cm}^{-1}$. Each sample is scanned about 120 times while generating the transmittance spectra. The chemical structure determination of a sample is mainly based on the molecular

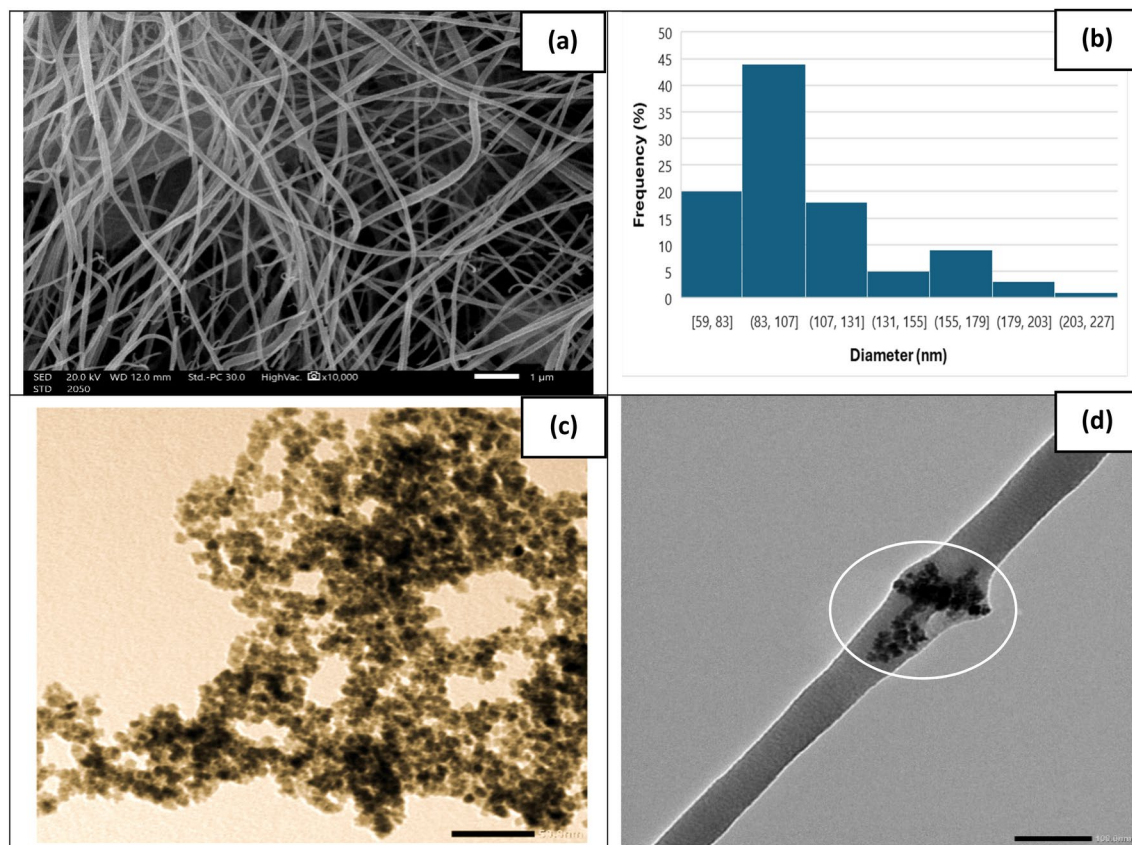


Fig. 4. Microscopic images of the ceria NPs and ceria embedded PVDF electrospun nanofibers: **(a)** SEM image of ceria embedded PVDF electrospun nanofibers in 2 μm scale, **(b)** Nanofibers diameter distribution curve of PVDF/ceria with ratio 95:5 wt%, respectively, **(c)** TEM image of ceria NPs in 50 nm scale, and **(d)** TEM image of 5% PVDF/Ceria.

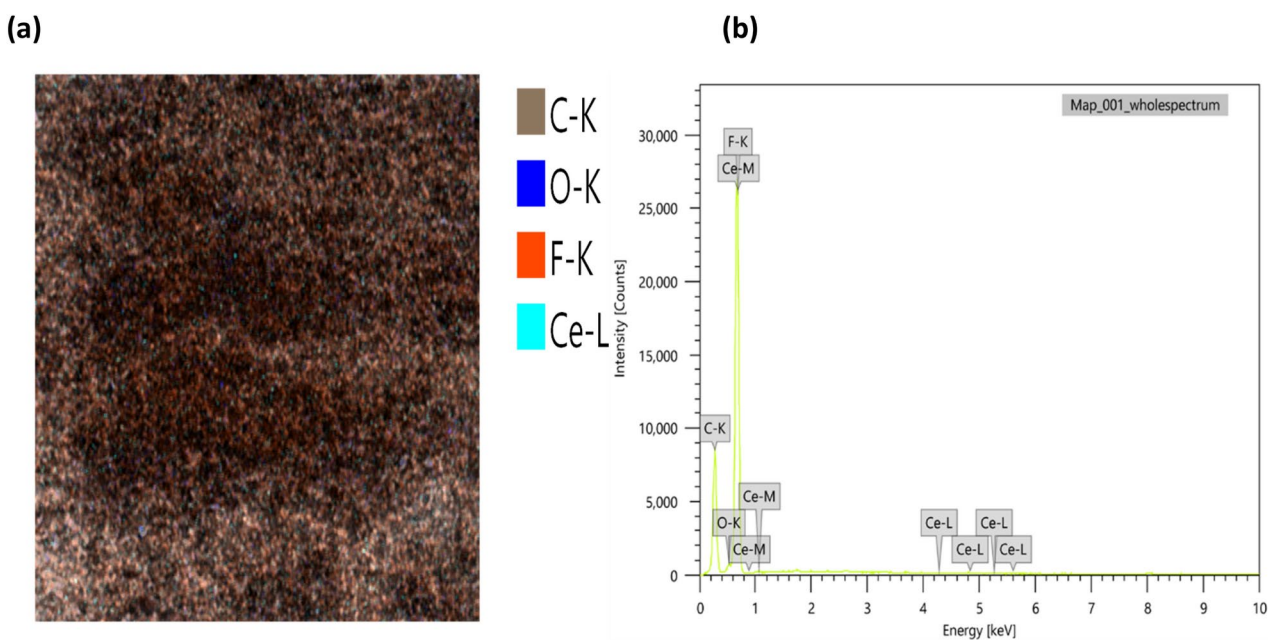


Fig. 5. **(a)** and **(b)** represent the EDS mapping of ceria 5% embedded PVDF electrospun nanofibers in 100 μm scale.

vibrations. Stretching and bending are the two types of molecular vibrations involved in IR spectroscopy. Stretching mode changes the bond length resulting in either symmetric or asymmetric mode whereas the bending mode always changes the bond angle. Whenever the frequency of a specific bond vibration becomes exactly equal to the frequency of the applied IR radiation, the radiation will be completely absorbed by the sample content generating a plot of transmittance (or absorbance) versus wavenumber. This FTIR spectroscopy can be widely used for both quantitative and qualitative analysis of nanoparticles and nanocomposites, especially polymer nanocomposites. Thus, IR spectroscopy can clearly identify the chemical structure of polymers and the nanoparticles and corresponding spectra can be generated⁶⁸.

The FTIR spectra of pure PVDF and PVDF/ceria composite membranes presented in Fig. 6 clear vibrational bands indicative of the molecular structure and phase transitions of PVDF, particularly in the α and β phases. Previous studies^{20,69,70} have reported characteristic vibrational bands between 481 and 488.53 cm^{-1} , corresponding to CF_2 bending in the nonpolar α phase, and at 527 cm^{-1} to 532 cm^{-1} , which also corresponds to CF_2 bending in the α phase⁶⁹. Additionally, bands at 618 cm^{-1} to 608.9 cm^{-1} and 758 cm^{-1} to 763 cm^{-1} represent CF_2 bending and skeletal bending in the α phase, while the bands at 796.8 cm^{-1} and 975.03 cm^{-1} are attributed to CH_2 rocking and CH_2 twisting, respectively, again corresponding to the α phase. Furthermore, bands between 507 and 512.6 cm^{-1} and around 830.5 cm^{-1} to 840.16 cm^{-1} indicate the β polar phase⁷¹, and their appearance is linked to the ceria-induced enhancement of the β phase in PVDF/ceria composites. These findings support the crystallization of the β phase in the composite materials.

Despite the extensive FTIR studies, previous works^{59,72–78} do not sufficiently explore the correlation between the phase composition of PVDF/ceria composites and their piezoelectric properties. The vibrational bands at 510 cm^{-1} , 840 cm^{-1} , and 1275 cm^{-1} , which characterize the piezoelectric β phase, have been observed but often without a detailed quantification of β -phase content in composites at various ceria loadings. Additionally, the relationship between these vibrational modes and the material's functional properties has not been fully explored in the context of ceria incorporation. This study aims to fill these gaps by systematically evaluating the FTIR spectra and applying Beer Lambert's law to calculate the β -sheet content in PVDF/ceria composites. Notably, our findings show that the β -sheet content in PVDF/ceria composites is maximized at a 5 wt% ceria loading, compared to lower ceria concentrations and pure PVDF. This work contributes to a deeper understanding of the influence of ceria on the crystallization of PVDF and provides a more precise link between Beta phase formation and material functionality in terms of piezoelectric properties.

The β sheets associated with the compositions can be calculated using the equation derived from Beer Lambert Law and is given by:

$$f(\beta) = \frac{A_{\beta}}{1.26A_{\alpha} + A_{\beta}} \quad (2)$$

where A_{β} represents the absorbance value at 840 cm^{-1} , and A_{α} represents the absorbance value at 766 cm^{-1} ^{79,80}.

Based on the calculations using Beer Lambert's law, the β sheet contents was found to be the highest for PVDF/ceria 5 wt% composition. In the case of pure PVDF, the β sheets was found to be maximum, compared

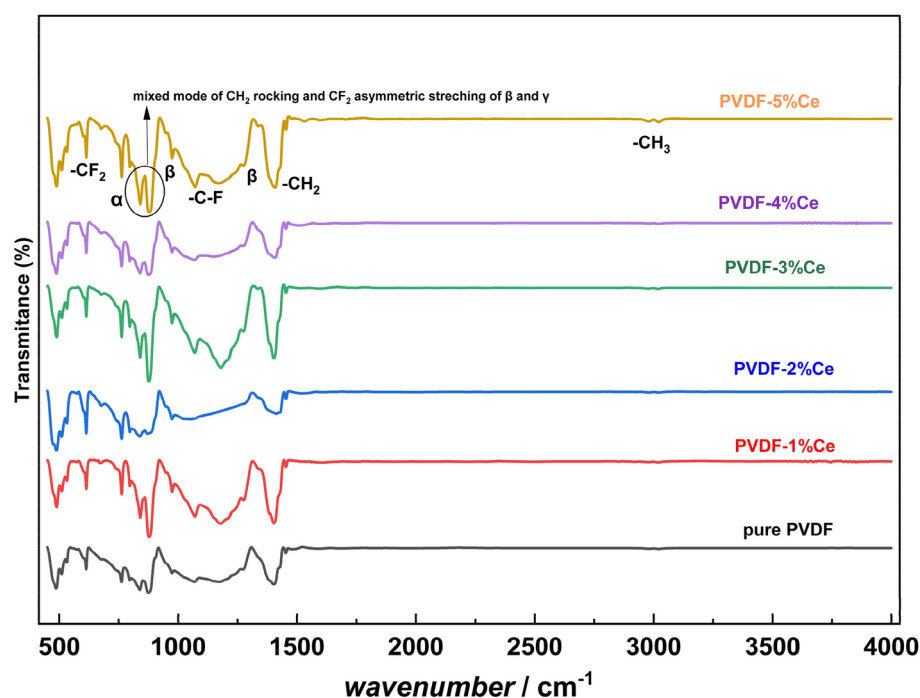


Fig. 6. FTIR spectra of pure PVDF and different PVDF/ceria compositions.

to all other compositions from 0.5 to 3 wt%. The β -sheet content percentage calculated for each concentration is mentioned in Table 1.

This clearly shows the enhancement of β sheets and piezoelectric effect by the addition of ceria NPs, and it is found that the effect of β sheets become prominent only above certain threshold ratio associated with percolation threshold and it is discussed in detail in the piezo characterization part⁶⁷. The addition of ceria NPs on to the PVDF polymer results in the reduction of crystallinity due to the accumulation of NPs and associated crystal defects. This may be the reason for reduction of β sheet contents in the PVDF/ceria composites for the ratio 0.5% to 4%. Above percolation threshold, the NPs get distributed uniformly resulting in an increase in the overall crystallinity. As a result, the PVDF molecular chains are forced to orient in TT conformation due to the generation of induced charges at the boundary. This TT conformation emerged from the uniform dispersion of ceria nanoparticles inside the polymer chains⁸¹.

Another band was observed at 1182.2 cm^{-1} , emerged only for the PVDF/ceria composition and absent in the pure PVDF sample. This band creation and broadening at 1182.2 cm^{-1} account for the enhancement of significant percentage of β phase. Due to CF–CH–CF bending vibration, a band is observed at 873.88 cm^{-1} , and it seems to be shifted to higher energy values up to 878.7 cm^{-1} . The shift of CF–CH–CF bending vibration towards higher energy is due to the increased specific interaction between the cerium NPs and PVDF chains⁸². A band observed at 1071.4 cm^{-1} corresponds to cerium co-ordinate complex formation and it is not present in the case of pure PVDF⁸³. Vibrational band observed at 1071.4 cm^{-1} mainly depends on the thickness of the nanocomposite membrane and almost linear dependence is there and has no direct dependence on the crystallinity of PVDF⁸⁴. A tiny shoulder at 1234 cm^{-1} is observed to be prominent in the case of PVDF/ceria composite which represents the generation of Υ phases. Also, the appearance of 833 cm^{-1} and 838 cm^{-1} bands accounts for the generation of Υ phases and finally the conversion of Υ to β by the addition of more quantity of ceria NPs. Very small vibrational bands observed in the region from 2974 to 3027 cm^{-1} in the FTIR spectra is mainly associated with symmetric ν_s (–CH₂) and asymmetric ν_{as} (–CH₂) stretching respectively. Furthermore, the electronegativity of carbon atom (2.5) differs a lot with fluorine atom (4.0) and as a result C–F polarised bond will be very strong compared to C–H bond. In case of C–H bond, the electronegativity between carbon and hydrogen (2.1) is very small and this results in the generation of a weak C–H bond compared to C–F bond and this is the reason for the stronger ion dipole interaction between positively charged surfaces of the additives and CF₂ dipoles of PVDF. Ion dipole interaction mechanism is clear from the FTIR spectra of pure PVDF and PVDF/ceria composites in our studies. In the case of pure PVDF, FTIR spectra clearly displays the C–F stretching vibration band at 876 cm^{-1} , but in the case of PVDF/ceria composite membrane, the C–F stretching vibration band is found to be shifted to 879 cm^{-1} (5% ceria case) which clearly explains the ion dipole interaction effect. This effect is strong enough to overcome the energy barrier that transforms α (TGTG) conformation to β (TTTT) conformation or Υ (TTTG) conformation. This acts as the base for polar phase generation in the PVDF crystallization process via nucleation and growth stages⁸⁵.

In general, polar phase generation in PVDF from its composites can be explained by the mechanism of ion–dipole interaction, provided charged substances are contained in the composites. In the case of PVDF, ion dipole interaction can occur due to the interaction between CH₂ dipoles in PVDF chains and negatively charged surfaces or CF₂ dipoles in PVDF chains can interact with the positively charged surface. Based on different studies, ion dipole is produced due to the interaction between positively charged surfaces and CF₂ dipoles of PVDF⁸⁵. Specifically, our studies focus on the effect of Ce³⁺ ion interaction with the CF₂ dipoles of PVDF and this results in the generation of polar phases in PVDF thereby enhancing its piezoelectric property.

X-ray diffractograms of Pure PVDF, and PVDF blended with varying percentages of Ce (1%, 2%, 3%, 4%, and 5%) were recorded in a Bruker D8 advanced diffractometer using CuK α radiation with a wavelength of 0.15406 nm. Spectra were registered between 10° to 90° (2 θ) with a step of 0.1° and a time per step of 3 s. Indexation of the patterns was accomplished using dedicated software (DIFFRAC.EVA) from Bruker.

The XRD pattern of the pure PVDF film in Fig. 7 shows three strong diffractions at $2\theta = 18.7^\circ$ and 26.6° , corresponding to the characteristic (020) and (021) diffractions of the α -phase⁸⁶. Alternatively, the $2\theta = 21.2^\circ$ and 36.8° peaks are mainly ascribed to the characteristic (110) and (020) diffractions, respectively, for the β -phase⁸⁷.

Notably, a moderate enhancement of the (110) peak of the β -PVDF phase can be observed with the addition of Ce. Moreover, the intensity at $2\theta = 18.7^\circ$ decreased, and $2\theta = 26.6^\circ$ almost disappeared, confirming the change of α -phase toward more β -phase (020) at 36.8° .

Table 2 presents the Bragg angle values of 2θ (°), the inter-planar distance $d(\text{Å})$, and the crystal size $L(\text{Å})$ according to the three β -phase peaks observed in the diffractograms (Fig. 7), which was calculated by Scherrer Eq. (2)⁸⁸.

$$L (A) = k\lambda/\beta \cos \theta \quad (3)$$

Ceria NPs %	A(α)	A(β)	f(β)
0	1.44	2.55	58.41
0.5%	0.87	1.27	53.7
1%	0.38	0.57	54.64
3%	0.37	0.57	55.49
5%	0.55	1.11	61.75

Table 1. Calculated β -phase content percentage of PVDF/ceria nanocomposite nanofibers.

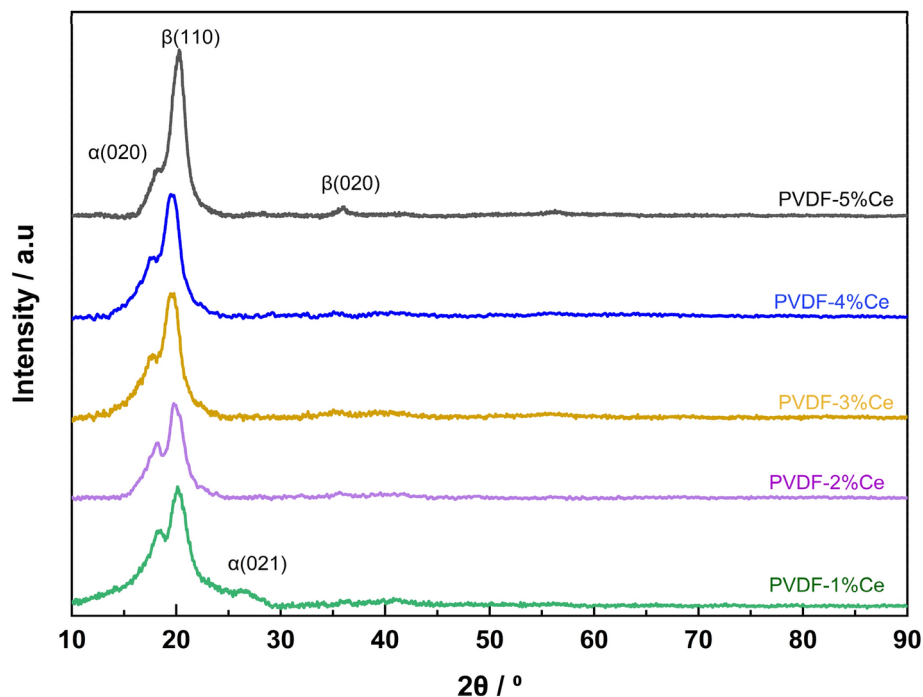


Fig. 7. XRD results of PVDF with different wt% Ceria.

Sample	β-phase (020)		
	2θ (°)	D (Å)	L (Å)
PVDF	36.6	1.20	20.34
PVDF-1%Ce	36.8	1.20	22.07
PVDF-2%Ce	36.8	1.20	23.54
PVDF-3%Ce	36.9	1.20	24.43
PVDF-4%Ce	37.0	1.20	26.12

Table 2. The Bragg angle values of 2θ (°), the inter-planar distance d(Å), and the crystal size L(Å) of the PVDF and PVDF blended with different Ce%

L: Crystallite size (in Å) or nanometers), K: Scherrer constant = 0.9, λ: X-ray wavelength (Å), β: Full width at half maximum (FWHM) of the diffraction peak and θ: Bragg angle corresponding to the peak in the XRD pattern (°).

The XPS results for PVDF with 5 wt% ceria reveal distinct peaks corresponding to key elements. The C 1s spectrum shows peaks at ~284.5 eV and ~290 eV, indicating the presence of C–C, C–H, and C–F bonds characteristic of PVDF. The F 1s spectrum exhibits a sharp peak around ~688 eV, confirming the presence of fluorine from PVDF⁸⁹. The O 1s spectrum (bottom left) displays a broad peak around ~530–535 eV, suggesting multiple oxygen states, possibly from surface hydroxyl groups and lattice oxygen in ceria⁹⁰. The Ce 3d spectrum exhibits a broad, asymmetric shape without significant splitting. The absence of distinct Ce 3d splitting suggests strong hybridization between Ce and O, typical of CeO₂⁹⁰. Thus, while XRD and XPS are powerful tools, the small nanosized CeO₂ crystal, as confirmed by TEM, made it difficult to detect (Fig. 8).

Microwave digestion was carried out using Milestone's ETHOS UP system. A small amount of sample (25.000 mg) of PVDF-5% Ce was accurately weighed, and 8 mL of concentrated HNO₃ and 3 mL of concentrated H₂SO₄ were added. The vessels were heated to 210 °C in 25 min at 1800 W, maintained for 15 min before cooling down. The solution was then transferred to a 50 mL flask and diluted with 1% HNO₃ prepared in MQ water. The solutions were filtered through a 0.45 μm nylon filter. The concentration of Ce ions was determined using Agilent 5100 ICP-OES. Five replicates of the sample were analyzed. The coefficient of variation of the method is 1%. Inorganic Ventures VAR-CAL 1 standard (was used to prepare mixed-metal calibration standards in the range of 1–1000 μg L⁻¹ in MQ water (> 18 MΩcm) were analysed. The Ce ions concentration was 1.70 mg/g, and the Standard deviation (SD) was 0.03 mg/g. The actual Ce content in the sample might be higher than measured due to incomplete dissolution of the sample. The post-digestion solution analysis showed a significant presence of cerium, indicating that the digestion process successfully extracted Ce from the dissolved portion, but some Ce may have remained in undissolved residues, leading to an underestimation in the ICP results and there is no possibility for mineralization. There, Ce in PVDF-5%Ce, as shown in Fig. 9 was examined using an Energy-Dispersive X-ray fluorescence spectrometer (XRF, ARL QUANT'X, Thermo Scientific, Waltham, MA,

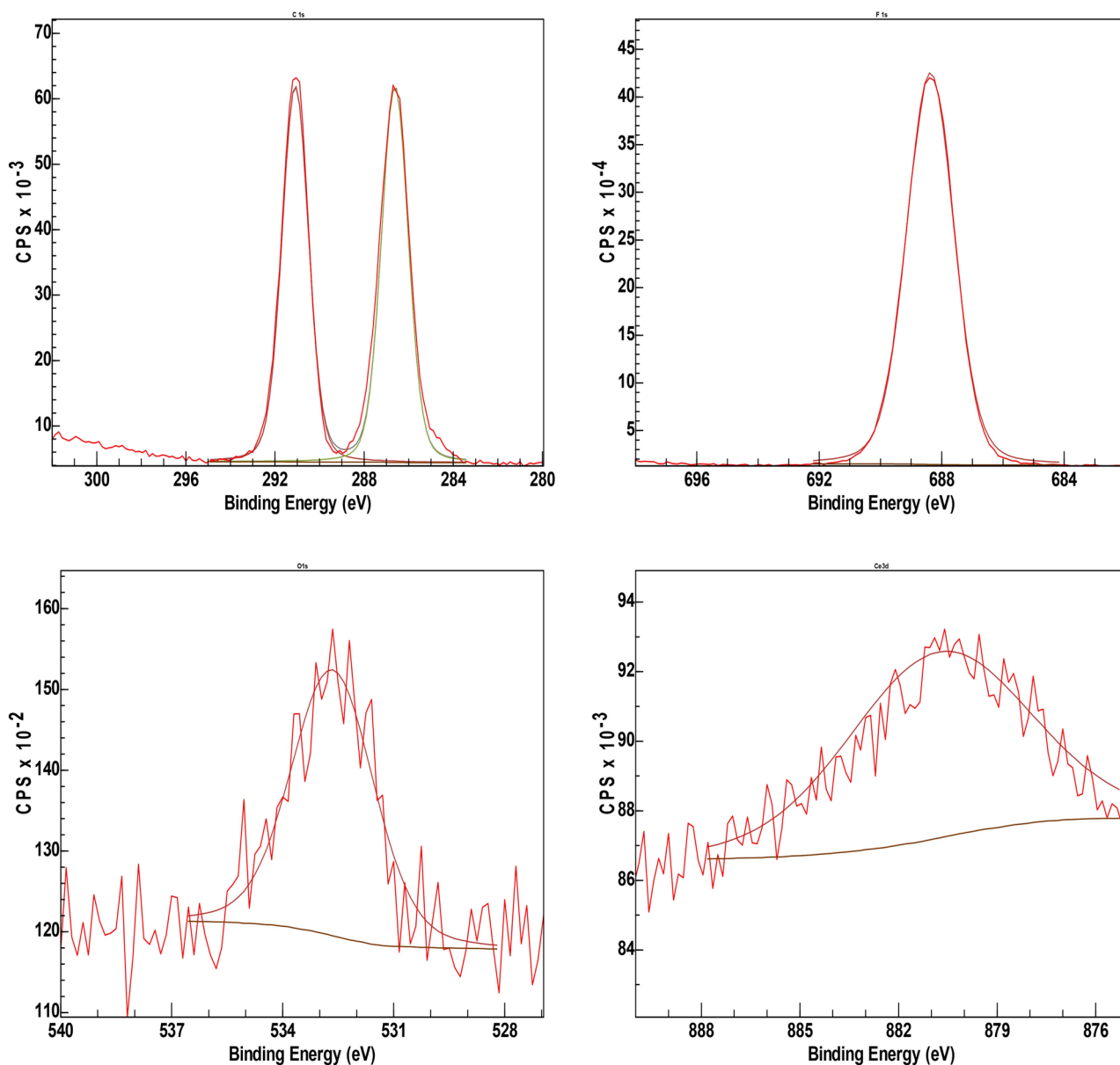


Fig. 8. XPS results of PVDF with 5 wt% Ceria.

USA), with a Rhode-anode as a source of X-rays and a detecting system of Si(Li) crystal with Peltier cooling. The surface of PVDF-5%Ce sample contains a significant amount of CeO_2 .

The effect of ceria doping over PVDF surface is investigated by Raman spectroscopy. a handheld Raman spectrometer (a Renishaw Raman microscope 2000 system) equipped with a 785 nm laser was used to obtain the Raman spectra of pure PVDF and PVDF doped with 5%Ce. both spectral measurements used the following experimental parameters: an excitation wavelength of 785 nm, an acquisition time of 60 s, a laser power of 5 mW, a spectral resolution of 4 cm^{-1} , and a spectral range of $250\text{--}3200 \text{ cm}^{-1}$. Each spectrum was the average of five scans obtained from the different spots of the PVDF surface for the 2 samples. Savitzky–Golay smoothing filter is used to minimize fluorescence noise. The area under the alpha and beta peak in Raman was calculated by Gaussian Function. The Raman spectra of PVDF and ceria/PVDF are shown in Fig. 10. The Raman fingerprints appeared at 794 cm^{-1} and 839 cm^{-1} are due to PVDF matrix. The α -phase PVDF shows a sharp peak at 794 cm^{-1} , which is due to the rocking of the CH_2 bond, whereas the band at 839 cm^{-1} is attributed to the β -phase^{91,92}. The band around 1431 cm^{-1} is caused by bending CH_2 vibrations, present in both crystalline phases of PVDF but mainly in the β - phase⁹³. The band at 2974 cm^{-1} is usually attributed to CH_2 symmetric stretching commonly associated with the β -phase⁹⁴. The transition to the β -phase can be monitored by comparing the relative intensities of the bands at ca. 794 cm^{-1} and 839 cm^{-1} after adding 5 wt% ceria to PVDF. The intensity of the peak at 839 cm^{-1} sharply increases, revealing the β -phase's appearance. Conversely, the characteristic band α decreases in intensity in favor of the β band. This observation is directly related to the conformational transformation of the macromolecular chain generated by the addition of 5% Ce.

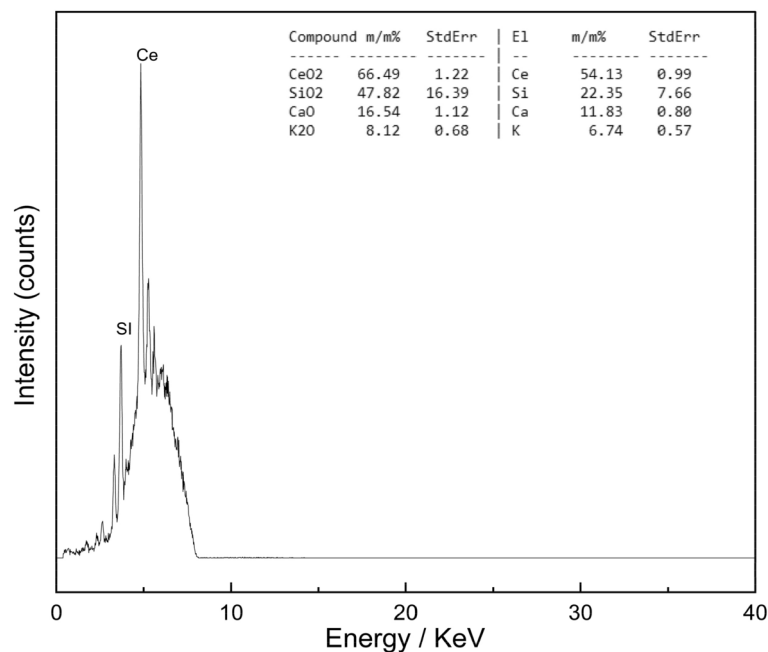


Fig. 9. XRF spectra of pure PVDF and PVDF with 5 wt% ceria NPs.

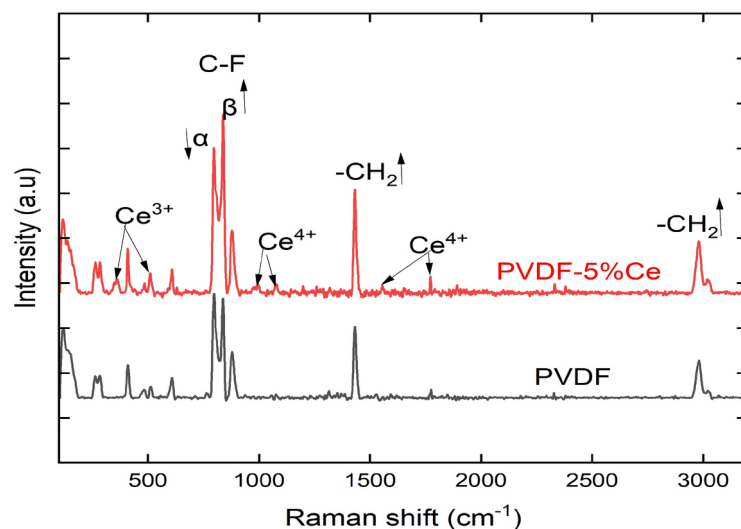


Fig. 10. Raman spectra of pure PVDF and PVDF with 5 wt% ceria NPs.

The exact quantity of transformation is presented in both Fig. 11 for both pure PVDF and PVDF doped with 5 wt% ceria, respectively, by using Gaussian fitting. The primary goal of Raman peak by Gaussian fitting is to determine quantitatively crystalline phases depending on the peak parameters such as peak position, intensity, area, and width. The fractions of the crystalline phases are measured from the integration method of the representative peaks of the different phases (794 and 839 cm^{-1}). The estimation of the fraction of α -phase in the total crystalline phase is calculated according to Equation.

$$F(\beta) = \frac{\sum A_{\beta \text{Gaussian}}}{\sum A_{\alpha \text{Gaussian}} + \sum A_{\beta \text{Gaussian}}} \quad (4)$$

where $A_{\alpha \text{ Gaussian}}$ and $A_{\beta \text{ Gaussian}}$ are areas calculated after integration of corresponding Gaussian peaks. Pure PVDF contained 70.07% α -phase and 29.93% β -phase. However, the α -phase decreased to 50.78%, and the β -phase increased to 49.22% after adding up to 5 wt% of ceria. Raman spectroscopy was also used to investigate the presence of Ce^{3+} species. Raman spectrum of the PVDF doped with 5% Ce confirms the appearance of new bands at 369 and 514 cm^{-1} , which corresponds to $\text{CeO}_2(\text{Ce}^{3+})$ of Ce-O lattice^{95,96}. Moreover, the band at

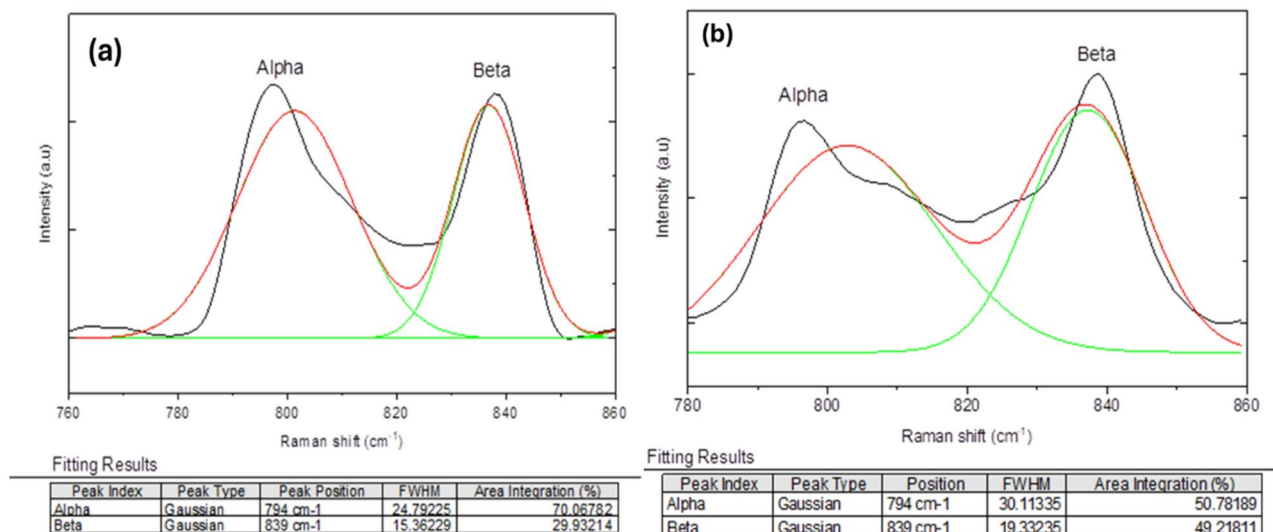


Fig. 11. Gaussian fitting of Alpha and Beta peaks in pure PVDF (a) and in PVDF with 5 wt% ceria (b).

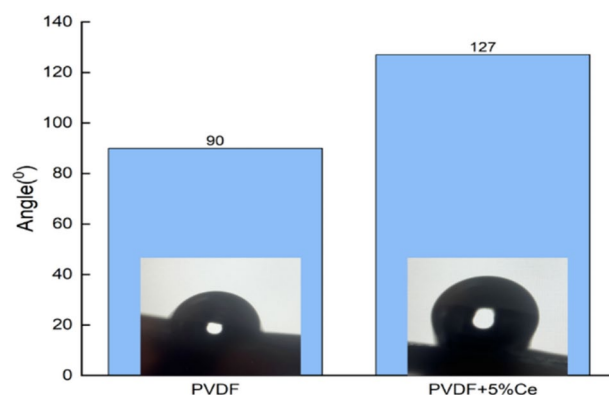


Fig. 12. The contact angle of the water drop over pure PVDF and PVDF with 5 wt% ceria.

999, 1074, 1565 and 1770 cm⁻¹ are attributed to the CeO₂(Ce⁴⁺)⁹⁵. The redox cycling between Ce³⁺ and Ce⁴⁺ is basically governed by creating a surface oxygen vacancy in CeO₂ due to the reduction of Ce⁴⁺ to Ce³⁺ and incorporation of negatively charged oxygen species in CeO₂ by oxidation of Ce³⁺ to Ce⁴⁺. However, such oxidation of Ce³⁺ to Ce⁴⁺ is the reason of the presence of Ce⁴⁺. The presence of a significant fraction of Ce³⁺ on surface promotes a more active interaction of ceria with PVDF with the new β-phase formation, which agrees with the IR spectroscopy data. As a further matter, the presence of Ce³⁺ enhances the band intensity of CH₂ at 1431 cm⁻¹ and 2974 cm⁻¹, which is attributed to the new β-phase formation and the increase in the hydrophobicity of the sample⁹⁷.

The wettability properties of the pure PVDF and PVDF doped with 5% Ce are studied by contact angle measurements at room temperature and under air atmosphere. Using the drop shape analysis-profile device with a tiltable plane (DSA-P, Krüss, Germany), advancing the average of 6 contact angles of water contact angles. Initially, a 15 μL drop of ultrapure water is applied to the surface of PVDF and PVDF doped with 5% Ce sample using a variable-volume syringe. After that, the sample that was supporting the drop was tilted at a steady rate (1°/s), and photos of the drop is concurrently captured. The bouncing level of the water drop on the surface of pure PVDF, and PVDF doped with 5% Ce was considered as a measure of the hydrophobicity level. As shown in Fig. 12, the contact angle is 90 ± 2° for pure PVDF, but it climbed to a high of 127 ± 2° upon addition of 5% Ce. Similar results were obtained by Salah et al.⁹⁸, who observed the super hydrophobicity behavior of PVDF after introducing CeO₂ nanoparticles. Introducing Ce into PVDF leads to a change in the chemical conformation and crystallization which causes a change of surface energy and consequently induces a change of surface wettability. After doping PVDF with 5%Ce, many nano-sized asperities of Ce were generated on the surface, which increased the layer roughness. According to the Cassie–Baxter hypothesis⁹¹, the air trapped by the nanosized asperities can change a solid–liquid contact surface into water droplets. The other explanation of the CeO₂ hydrophobicity is based on its electronic structure. Valence electron orbitals of CeO₂ are protected by the electron octet 2s²2p⁶ of

crystalline oxygen, which makes the water drop hard to build chemical bonds with the surface. Therefore, it is clearly confirmed that nanostructures CeO_2 are incorporated in the PVDF polymer.

Piezoelectric properties of the PVDF/ceria nanofibers membrane

The piezoelectric performance of the fabricated nanofiber mats towards different mechanical disturbances in the form of compressive loads/forces are analysed. The peak-to-peak output voltage generated from the nanofibers mat is measured using a high impedance Oscilloscope (Tektronix MDO3014). Prior to testing the samples under various mechanical excitations, they were positioned between two aluminium foil sheets serving as metal electrodes. The potential output generated from the electrodes was captured through stainless steel wires. The output from these wires was directed to the oscilloscope, allowing for the visualization of the generated peak-to-peak voltage.

Voltage based characterization

When a strain or force is applied onto the flexible PVDF/ceria nanofibers mat, the crystal structure of nanofibers is highly deformed resulting in an effective piezoresponse development, and this potential is detected through the electrode ends of the piezomat. The piezoelectric potential corresponding to the mechanical impacts are pulsed voltages and the ac sinusoidal voltage produced by different PVDF/ceria concentrations at a specific force of 3 N is shown in Fig. 13.

For force voltage analysis, a force of 0.5 N to 3.5 N is applied onto the PVDF/ceria nanofibers membrane and the corresponding output voltage is recorded. For each concentration the output voltage is found to be increasing linearly. By analysing the voltage versus force graph for PVDF/ceria nanofibers for different concentration from 0 to 5%, its clearly visible that the piezoresponse is enhanced for 3% and 5% concentration. In the case of 0.5% and 1% ceria, the piezoresponse is not found to be improved and it is found to be weaker than pure PVDF.

The relation between voltage and applied forces for different ceria concentrations are shown in Fig. 14a. This is because the addition of NPs up to a certain level below the percolation threshold can decrease the crystallinity and can limit the enhancement of piezoresponse. Thus, based on the impact of compressed loads, its clearly proved that the piezoresponse can be improved by the addition of ceria NPs and the electroactive phase generation is found to be optimum for 3 to 5 wt% concentration. Below this concentration, even the polar phase generation is inhibited resulting in a weak piezoactivity, which was verified from FTIR spectra also. For 5% concentration of ceria, even the ion–dipole interaction effect is clearly pronounced, thereby showing a shift in the C–F stretching vibration band. Here, there is interfacial interaction between PVDF dipoles and NPs. The surface of ceria NPs usually contains positive charge verified from Zeta potential⁹⁹. This positive charge can contribute to the electroactive phase formation in PVDF by ion dipole interaction process. The positive charge cloud or the positive ion responsible for ion dipole interaction in the present study is Ce^{3+} ion of ceria. Thus, polar phase generation in PVDF from its composites containing charged substances can be achieved by utilising the mechanism of ion dipole interaction. Here the TGTG(α) conformation is easily changed to TTTT(β) or TTTG(γ) conformation by overcoming the energy barrier during PVDF crystallisation¹⁰⁰. The electrostatic interaction between the fluoride of PVDF and the positive charge cloud of the dopant (ceria) is shown in Fig. 14b, which has an efficient surface activity that results in an effective piezoresponse enhancement in the nanofibers composite membrane¹⁰¹. The electrostatic interaction is mainly related to hydrogen bonding and bipolar interactions between the PVDF and the cerium dopant's opposing poles. Notably, the piezosensitivity of the composite nanofibers has improved significantly without requiring any electric poling. A comprehensive investigation has explored the role of electrostatic interaction and hydrogen bonding arising from the protons on the surface of the cerium complex and the induced negative pole within the polymer chain. Therefore, intermolecular hydrogen bonding between the opposing poles of the matrix also enhances the interaction among the induced dipoles in the PVDF matrices. Additionally, along with the formation of the β phase, self-poling induced by hydrogen bonding occurs due to the charged vacancies in our synthesized non-stoichiometric ceria

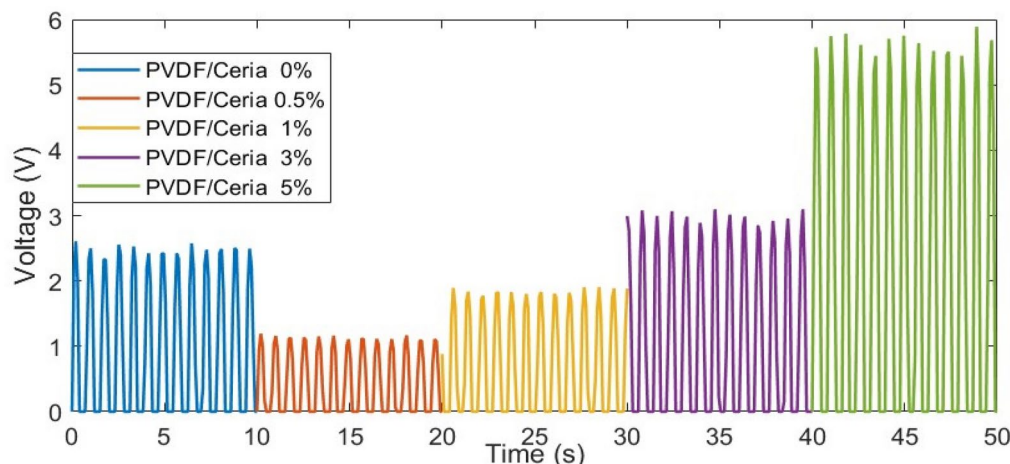


Fig. 13. AC sinusoidal voltage developed at 3 N force for different PVDF/ceria concentrations.

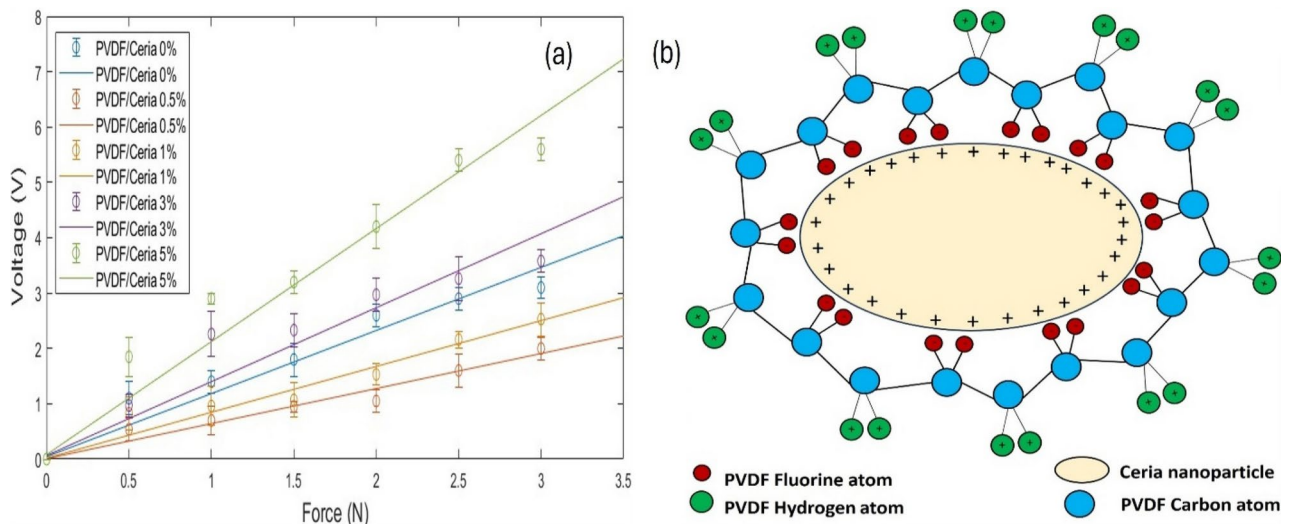


Fig. 14. (a) The peak-to-peak output voltage generated by the piezomats for different applied forces/compressed loads, and (b) Schematic representation of the dipole alignment of PVDF according to nucleating agent of ceria NPs.

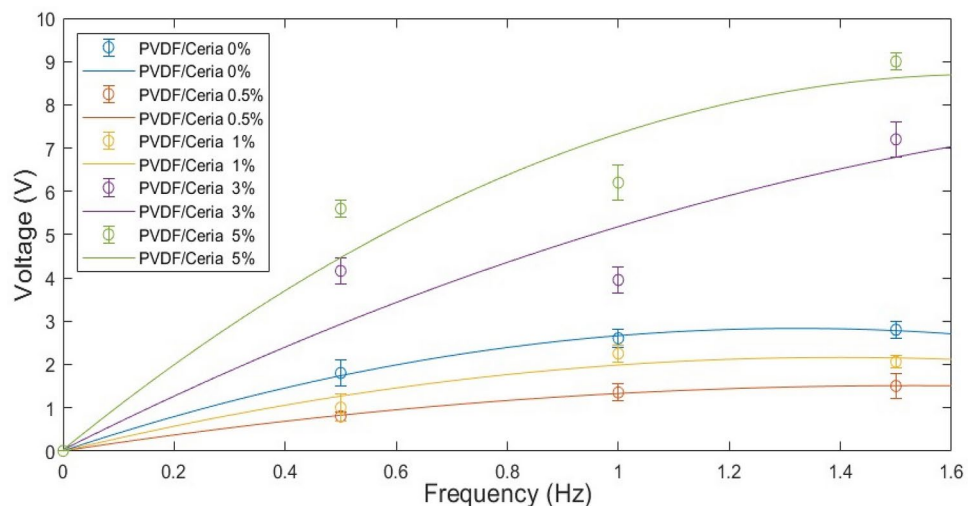


Fig. 15. The peak-to-peak output voltage generated by the piezomats for an applied force of 3N for different mechanical frequencies.

(CeO₂-x), which further strengthens the PVDF dipole moments aligned. Thus, in general, PVDF ceria complex-based nanofibers can be considered as a layer by layer pattern of non-centrosymmetric ceria encapsulated in beta phase generated PVDF matrixes. The application of an external uniaxial pressure on to the PVDF ceria composite nanofibers results in an overall deformation leading to an induced electrical potential difference between top and bottom surface of the nanofibers and finally an enhanced piezoresponse is observed³⁹.

The frequency response analysis is also done for each concentration, and it is found that the piezo response has increased with a frequency from 0.2 to 1 Hz finally showing a saturation behaviour at 1.5 Hz. A compressed load of 3 N is applied on to the sample nanofibers mat and the mechanical frequencies are varied. Ceria concentration of 0.5–1 wt% has shown a relatively weak piezo behaviour, compared to pure PVDF even for all the frequency values. The impulse response increases linearly while the frequency response increases with saturation behaviour at 1.5 Hz. The relation between voltage and applied frequencies for different ceria concentrations are shown in Fig. 15.

This clearly indicates that the piezo enhancement effects based on additive are always based on the optimum concentration and not for all concentration. For higher concentration such as 6%, the presence of NPs affected the nanofibers morphology and as a result bead formation was initiated. So, the piezo characterization of the nanocomposite sample was done for the optimized concentrations from 0 to 5% only. These nanofibers based

on PVDF with ceria has shown an exceptional piezo characteristic and thus can be effectively utilized for energy harvesting and sensor/actuator applications.

Power density and current density characterization

Piezoelectric potential developed across different load resistances are analysed. Here different load resistances in the range of 1.2–3.9 M Ω are applied across the positive and negative electrodes of the nanofibers mat and finally the electrodes are connected to the oscilloscope probe for visualizing the generated voltage. The power output corresponding to each load is measured by taking the ratio of the square of piezo voltage to the resistance (V^2/R). The area of impact is calculated and the ratio of power output to the area of the impact represents the power density. A circular head with an effective radius of 1.4 cm is used for the mechanical excitation. Finally, power density is plotted (Fig. 16) against the resistance loads to show the piezo efficiency of these nano mats. Then the current density is calculated by using the following equation¹⁰²:

$$I_D = \frac{P}{V.A} \quad (5)$$

where I_D is the current density of piezomats, P is the power, V is the output voltage while changing the resistance, and A is the area of our nanofibers.

Detailed analysis based on different ceria concentrations from 0.5 to 5% showed the effective behaviour of 3 to 5 wt% ceria concentrations. 0.5% to 2% ceria NPs concentration comparatively showed a weak response towards piezoefficiency. Power density plots of the piezomats exhibited a Lorentzian behaviour where maximum value is obtained for the resistance load 2.2 M Ω and 2.7 M Ω . The power density values are found to be decreasing gradually for the load resistances 3.3 and 3.7 M Ω and the corresponding plot is shown in Fig. 16. A maximum power density of 89 mW/m² is obtained for the optimum concentration of PVDF/ceria nanofibers mat. In addition, for 5% ceria, the current density gradually declined with increasing resistance, decreasing from approximately 9 mA/m² at 1.2 M Ω to 3 mA/m² at 3.7 M Ω .

P–E curve characterization (Sawyer Tower circuit)

To verify the piezoelectric characteristics of any material, determine the polarization–electric field hysteresis loop, which is regarded as one of the most important indications of the material's ferroelectric properties, such as the dielectric constant and electromechanical coupling coefficient¹⁰³. The Sawyer–Tower circuit is one of the most powerful tools for determining the loop¹⁰⁴. As demonstrated in supplementary file Figure S5. This circuit contains two capacitors: one for the sample capacitance and one for a reference capacitor with a higher value. And an applied voltage of up to 2.5 kV at a frequency of 1.4 kHz, accomplished by amplifying the voltage from a signal generator with a step-up transformer. The collected data is then processed to determine the applied electric field (E) by using Eq. (6).

$$E = \frac{V_{in}}{d} \quad (6)$$

where V_{in} is the applied voltage, and d is the sample thickness.

Now, the electric polarization P is calculated according to Eq. (7), as follows.

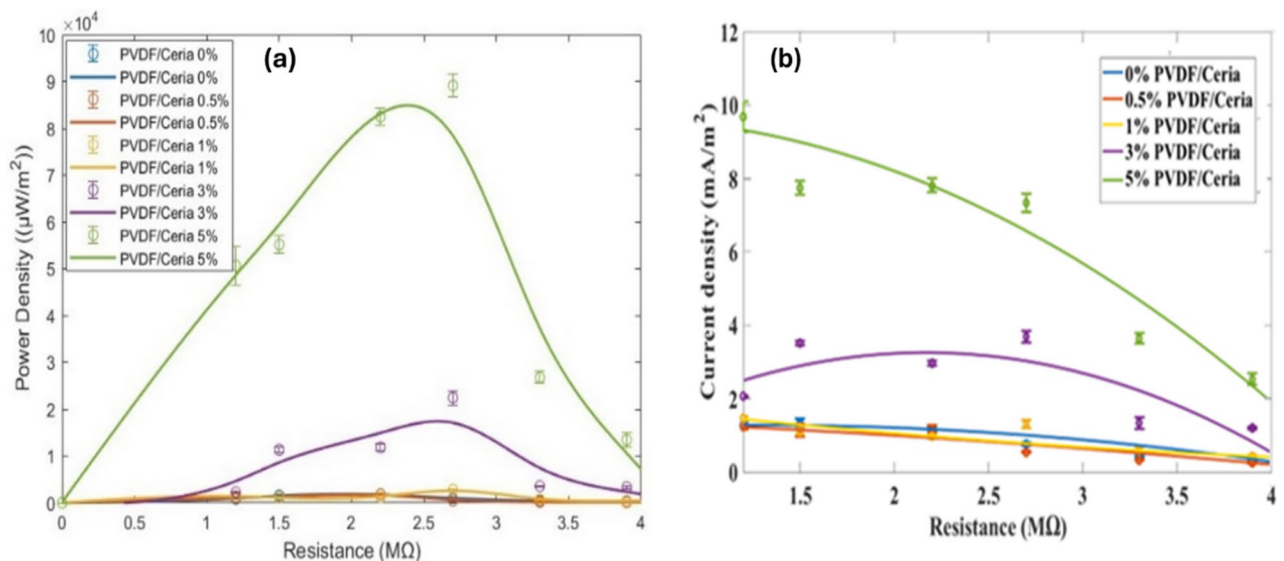


Fig. 16. Shows the relationship between (a) power density and load resistances for the piezomats, and (b) Current density and load resistances for the piezomats.

$$P = \frac{Q}{A} \quad (7)$$

where A is surface area, and Q is the charge on the sample capacitor. As a result, the P-E curve is obtained by using a high impedance oscilloscope (Tektronix MDO3014).

Ferroelectric properties of the sample were determined using a hysteresis loop between P and E as shown in the below mentioned Fig. 17. From the measurements, the sample had a coercive field (E_c) of about 45 kV/mm, indicating the electric field that must be applied to switch the polarization. Here, the remnant polarization (P_r) was read at about $0.15 \mu\text{C}/\text{cm}^2$, which refers to the remaining polarization after the electric field has been swept away, while the maximum polarization attained about $0.3 \mu\text{C}/\text{cm}^2$ under the sweep of an applied electric field. Such values indicate that the material is strongly ferroelectric and hence well-suited for numerous applications. The remnant polarization is large, while the coercive field is moderate. Our sample performs competitively, which is attributed to the optimized synthesis process and uniform dispersion of nanoparticles in the polymer matrix. The results underline its potential in advanced ferroelectric and piezoelectric applications.

The presence of nanoparticles within a structured polymer reduces unwanted particle aggregation and increases robust interactions between the host matrix and NPs involved. Here, PVDF acts as a capping agent and ceria NPs acts a nucleating agent for the PVDF electroactive phase¹⁰⁵. In summary, the surface energy of the prepared ceria NPs is high and as a result they are thermodynamically unstable. When these NPs are added onto the PVDF matrix, the surface energy stabilization occurs due to adsorption of capping ligand PVDF on the surface and thus electrostatic interaction stabilises the nanoparticles. This affects the crystallisation of PVDF reducing the molecular mobility inside the polymer layer close to the surface of the nanoparticle, and by the polymer chain orientation using the additive and obviously by the increased nucleation rate¹⁰⁶.

Electrospun PVDF nanofibers with certain additives/nanofillers greatly improved the piezosensitivity and electroactivity of the prototypes and the effect of some of them that has been published before is briefly summarized in Table 3 and compared with the present work. The electrospinning parameters used to generate those prototypes are also mentioned in the table and compared with the current study. Brief analysis based on different nanofillers clearly shown the effective presence of those additives in enhancing the piezoelectric behavior of pure PVDF electrospun nanofibers. Among the additives, ceria an optically active additive not only improved the piezoactivity but also exhibited enhanced optical activity.

Conclusion

In this study, we've engineered a new composite membrane comprising inorganic-organic nanofibers, integrating varying concentrations of the inorganic ceria additive into the organic polymer PVDF. Optical characterization via absorbance analysis revealed a blue shift in the ceria NPs' band gap, concurrently enhancing UV absorption in the PVDF polymer. Luminescence analysis showcased an incremental fluorescence effect at certain additive concentrations. However, beyond a specific threshold, further increments led to reduced fluorescence due to apparent quenching effects. FTIR analysis of the composite nanofibre membrane showed an increase in β sheet content with (PVDF- 5% ceria) with an average nanofibre diameter of 70.43 nm. Likewise, Raman and XRD results indicate a boost in β sheet content with the same concentration of ceria NPs. Additionally, the ICP and XRF data confirm a significant concentration of Ce incorporated with PVDF chain, supporting the effectiveness of the preparation methods used for depositing Ce in the PVDF fibre.

Piezoelectric characterization, based on applied loads, demonstrated a twofold enhancement in efficiency at the 5% ceria concentration, resulting in a threefold increase in voltage generation under cyclic force at 1.5 Hz. The resultant PVDF/ceria nanomembrane exhibited a remarkable maximum power density of $89 \text{ mW}/\text{m}^2$, evidencing its effectiveness in handling loads. This multifunctional nanocomposite, an outcome of PVDF/ceria complex electrospun fabrication, not only boasts optical fluorescence enhancements but also demonstrates

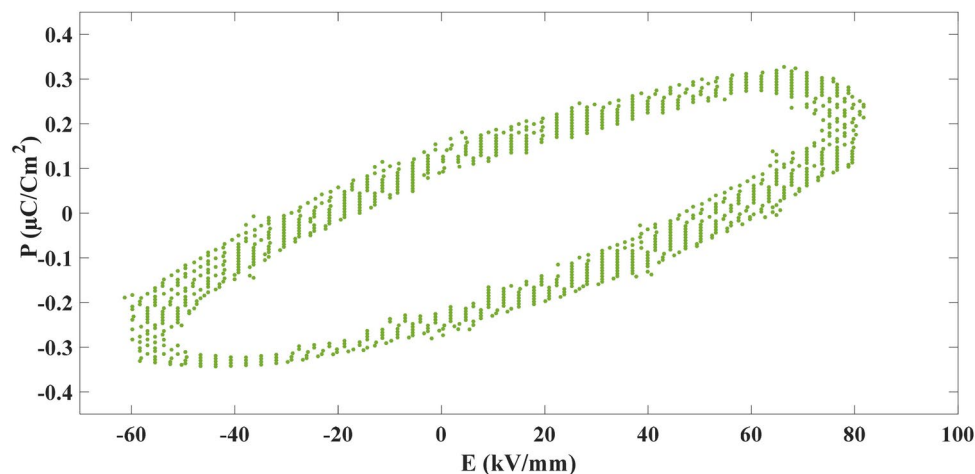


Fig. 17. Shows the P-E Hysteresis loops for 5% PVDF/Ceria.

Additives/fillers	Electrospinning parameters used	Mechanical excitation	Piezoelectric output parameter- V_{\max}/d_{33} /piezosensitivity	Reference
PVDF with 1 wt% Ag nanoparticles	HV—20 kV Feed rate—0.05 mL/hr Feed to collector distance—20 cm	d_{33} , FTIR characterization	d_{33} —27.1 Beta phase content—94%	24
PVDF-HFP with 2 wt% Co-ZnO nanofillers	HV—12 kV Feed rate—1 mL/hr Feed to collector distance—15 cm	Constant tapping force 2.5 N at 50 Hz	V_{\max} —2.8 V Beta phase content—54.6%	30
PVDF : TPU blending ratio 85 : 15 wt%	HV—25 kV Feed rate—1 mL/hr Feed to collector distance—10 cm	1–3 N compressed force at 8 and 16 Hz frequency Impulse loading (5 cm height) (20–150 g)	Sensitivity at 8 Hz—700 mV/N and at 16 Hz—300 mV/N V_{\max} —3.6 to 3.7 V at 85:15 PVDF:TPU ratio	79
PVDF with Au nanocage- 0.01 wt%	HV—15 kV Feed rate—1 mL/hr Feed to collector distance—15 cm	2–5 Hz compressed force	18.3 V_{\max} Beta phase from 83.5% to 93.2%	107
PVDF-MWCNT-Cu	HV—18 kV Feed rate—1 mL/hr Feed to collector distance—15 cm	Impulse loading (7 cm height) 35 g	V_{\max} —6.7 V	26
PVDF with 2 wt% (Fe_3O_4 -GO) nanoparticles	HV—12 kV Feed rate—0.25 mL/hr Feed to collector distance—15 cm	Applied force	Sensitivity—1.75 mV/N	108
PVDF with 5 wt% ceria	HV—25 kV Feed rate—1 mL/hr Feed to collector distance—15 cm	Compressed force of 3N at 1.5 Hz frequency	V_{\max} —9 V Power density—89 mW/m ²	Present study

Table 3. A list of published articles on electrospun PVDF with additives based composite nanofibers.

improved piezoelectric responses upon ceria NPs integration. This versatile nanocomposite holds a promise attraction for applications in multifunctional devices, serving as both an optical sensor and an energy harvesting unit. The work's future focus is on applying this prototype to acoustic detection and energy harvesting devices, as well as biomechanical energy harvesting units and optical sensors.

Data availability

Data are available based upon a request sent by email to the corresponding author.

Received: 15 January 2025; Accepted: 9 April 2025

Published online: 23 April 2025

References

- He, Z., Rault, F., Lewandowski, M., Mohsenzadeh, E. & Salaün, F. Electrospun PVDF nanofibers for piezoelectric applications: A review of the influence of electrospinning parameters on the β phase and crystallinity enhancement. *Polymers* **13**, 174. <https://doi.org/10.3390/polym13020174> (2021).
- Ico, G. et al. Size-dependent piezoelectric and mechanical properties of electrospun P(VDF-TrFE) nanofibers for enhanced energy harvesting. *J. Mater. Chem. A Mater.* **4**, 2293 (2016).
- Zhang, J. et al. Recent developments of hybrid piezo-triboelectric nanogenerators for flexible sensors and energy harvesters. *Nanoscale Adv.* **3**, 5645. <https://doi.org/10.1039/d1na00501d> (2021).
- Mahapatra, S. D. et al. Piezoelectric materials for energy harvesting and sensing applications: Roadmap for future smart materials. *Adv. Sci.* <https://doi.org/10.1002/advs.202100864> (2021).
- Li, X., Sun, M., Wei, X., Shan, C. & Chen, Q. 1D piezoelectric material based nanogenerators: Methods, materials and property optimization. *Nanomaterials* **8**, 188. <https://doi.org/10.3390/nano8040188> (2018).
- Victor, F. S., Kugarajah, V., Bangaru, M., Ranjan, S. & Dharmalingam, S. Electrospun nanofibers of polyvinylidene fluoride incorporated with titanium nanotubes for purifying air with bacterial contamination. *Environ. Sci. Pollut. Res.* **28**, 37520 (2021).
- Ebnesajjad, S. 3 - Introduction to fluoropolymers A2 - Kutz, Myer BT - applied plastics engineering handbook. In *Plastics Design Library* 2nd edn (William Andrew Publishing, 2017).
- He, Q. & Briscoe, J. Piezoelectric energy harvester technologies: synthesis, mechanisms, and multifunctional applications. *ACS Appl Mater Interfaces* **16**, 29491–29520 (2024).
- Nishiyama, T. et al. Crystalline structure control of poly(vinylidene fluoride) films with the antisolvent addition method. *Polym. J.* **48**, 1035 (2016).
- Sukumaran, S. et al. Recent advances in flexible PVDF based piezoelectric polymer devices for energy harvesting applications. *J. Intell. Mater. Syst. Struct.* **32**, 746 (2021).
- Cerrada, M. L., Arranz-Andrés, J., Caballero-González, A., Blázquez-Blázquez, E. & Pérez, E. The β Form in PVDF nanocomposites with carbon nanotubes: Structural features and properties. *Polymers (Basel)* **15**, 1491 (2023).
- Kapat, K., Shubhra, Q. T. H., Zhou, M. & Leeuwenburgh, S. Piezoelectric nano-biomaterials for biomedicine and tissue regeneration. *Adv. Funct. Mater.* **30**, 1909045. <https://doi.org/10.1002/adfm.201909045> (2020).
- Wu, L. et al. Recent advances in the preparation of PVDF-based piezoelectric materials. *Nanotechnol. Rev.* **11**, 1386. <https://doi.org/10.1515/ntrev-2022-0082> (2022).
- Vijayakumar, R. P., Khakhar, D. V. & Misra, A. Studies on α to β phase transformations in mechanically deformed PVDF films. *J. Appl. Polym. Sci.* **117**, 3491 (2010).
- Mehta, P. P. & Pawar, V. S. Electrospun nanofiber scaffolds: Technology and applications. *Appl. Nanocompos. Mater. Drug Deliv.* <https://doi.org/10.1016/B978-0-12-813741-3.00023-6> (2018).
- Drakopoulos, S. X. et al. Flexible polymer-based nanodielectrics reinforced with electrospun composite nanofibers for capacitive energy storage. *ACS Appl. Polym. Mater.* **4**, 8203–8215 (2022).
- Al-Dhahebi, A. M., Saheed, M. S. M. & Mustapha, M. Effects of solution concentration on the synthesis of polyvinylidene fluoride (PVDF) electrospun nanofibers. *Mater. Today Proc.* **80**, 2119 (2023).

18. Xue, J., Wu, T., Dai, Y. & Xia, Y. Electrospinning and electrospun nanofibers: Methods, materials, and applications. *Chem. Rev.* **119**, 5298. <https://doi.org/10.1021/acs.chemrev.8b00593> (2019).
19. Liu, F., Hashim, N. A., Liu, Y., Abed, M. R. M. & Li, K. Progress in the production and modification of PVDF membranes. *J. Membr. Sci.* **375**, 1. <https://doi.org/10.1016/j.memsci.2011.03.014> (2011).
20. Elnabawy, E. et al. Piezoelectric PVDF/TPU nanofibrous composite membrane: Fabrication and characterization. *Polymers (Basel)* **11**, 1643 (2019).
21. Shehata, N. et al. Acoustic energy harvesting and sensing via electrospun pvdf nanofiber membrane. *Sensors (Switzerland)* **20**, 3111 (2020).
22. Gade, H., Nikam, S., Chase, G. G. & Reneker, D. H. Effect of electrospinning conditions on β -phase and surface charge potential of PVDF fibers. *Polymer (Guildf)* **228**, 123902 (2021).
23. Carreau, P. J. & Vergnes, B. Rheological characterization of fiber suspensions and nanocomposites. In *Rheology of Non-Spherical Particle Suspensions* (Elsevier, 2015). <https://doi.org/10.1016/B978-1-78548-036-2.50002-2>.
24. Wu, C. M. & Chou, M. H. Acoustic–electric conversion and piezoelectric properties of electrospun polyvinylidene fluoride/silver nanofibrous membranes. *Express Polym. Lett.* **14**, 103 (2020).
25. Ge, X. et al. Preparation of polyvinylidene fluoride-gold nanoparticles electrospinning nanofiber membranes. *Bioengineering* **9**, 130 (2022).
26. Selvan, R. T. et al. Enhanced piezoelectric performance of electrospun PVDF-MWCNT-Cu nanocomposites for energy harvesting application. *NANO* **15**, 2050049 (2020).
27. Ekbote, G. S., Khalifa, M., Mahendran, A. & Anandhan, S. Cationic surfactant assisted enhancement of dielectric and piezoelectric properties of PVDF nanofibers for energy harvesting application. *Soft Matter* **17**, 2215–2222 (2021).
28. Du, X. et al. Porous, multi-layered piezoelectric composites based on highly oriented PZT/PVDF electrospinning fibers for high-performance piezoelectric nanogenerators. *J. Adv. Ceram.* **11**, 331–344 (2022).
29. Chamankar, N., Khajavi, R., Yousefi, A. A., Rashidi, A. & Golestanifard, F. A flexible piezoelectric pressure sensor based on PVDF nanocomposite fibers doped with PZT particles for energy harvesting applications. *Ceram. Int.* **46**, 19669–19681 (2020).
30. Parangusan, H., Ponnamma, D. & Al-Maadeed, M. A. A. Stretchable electrospun PVDF-HFP/Co-ZnO nanofibers as piezoelectric nanogenerators. *Sci. Rep.* **8**, 754 (2018).
31. Chandra, A., Prasad, S., Gigli, G. & del Mercato, L. L. Fluorescent nanoparticles for sensing. In *Frontiers of Nanoscience* Vol. 16 (Elsevier, 2020).
32. Wolfbeis, O. S. An overview of nanoparticles commonly used in fluorescent bioimaging. *Chem. Soc. Rev.* **44**, 4743. <https://doi.org/10.1039/c4cs00392f> (2015).
33. Kumar, S., Jain, G., Kumar, K., Singh, B. P. & Dhakate, S. R. A review on polymeric photoluminescent nanofibers: Inorganic, organic and perovskites additives for solid-state lighting application. *Polym. Sci. Ser. A* **64**, 367. <https://doi.org/10.1134/S0965545X22700213> (2022).
34. Kumar, S., Jain, G., Singh, B. P. & Dhakate, S. R. Tunable photoluminescence of polyvinyl alcohol electrospun nanofibers by doping of NaYF₄:Eu³⁺ nanophosphor. *J. Nanomater.* **2020**, 10235895 (2020).
35. Kumar, S. et al. A facile fabrication of poly(methyl methacrylate)/ α -NaYF₄:Eu³⁺ + tunable electrospun photoluminescent nanofibers. *Appl. Nanosci. (Switzerland)* **10**, 3875 (2020).
36. Kumar, S. et al. A novel fabrication of electrospun polyacrylonitrile/NaYF₄:Eu³⁺ light emitting nanofibers. *RSC Adv.* **10**, 24855 (2020).
37. Kumar, S. et al. Stress-induced structural phase transition in polystyrene/NaYF₄:Eu³⁺ photoluminescent electrospun nanofibers. *J. Nanomater.* **2022**, 2173629 (2022).
38. Shehata, N. et al. Fluorescent nanocomposite of embedded ceria nanoparticles in electrospun chitosan nanofibers. *J. Fluoresc.* **27**, 767–772 (2017).
39. Garain, S., Jana, S., Sinha, T. K. & Mandal, D. Design of in situ poled Ce³⁺-doped electrospun PVDF/graphene composite nanofibers for fabrication of nanopressure sensor and ultrasensitive acoustic nanogenerator. *ACS Appl. Mater. Interfaces* **8**, 4532–4540 (2016).
40. Breitwieser, M. et al. Cerium oxide decorated polymer nanofibers as effective membrane reinforcement for durable, high-performance fuel cells. *Adv. Energy Mater.* **7**, 1602100 (2017).
41. Alibe, I. M. et al. Polymer thermal treatment production of cerium doped willemite nanoparticles: An analysis of structure, energy band gap and luminescence properties. *Materials* **14**, 1–26 (2021).
42. Singh, K. R. B., Nayak, V., Sarkar, T. & Singh, R. P. Cerium oxide nanoparticles: Properties, biosynthesis and biomedical application. *RSC Adv.* **10**, 27194–27214. <https://doi.org/10.1039/d0ra04736h> (2020).
43. Tarasenko, N. et al. Nanoceria and hybrid silver–ceria nanoparticles fabricated by liquid-mediated laser ablation as antimicrobial agents. *Nano Struct. Nano-Objects* **34**, 100971 (2023).
44. Yadav, A., Mandal, J. R., Panda, A. B. & Shahi, V. K. Structural tailoring of ceria nanoparticles for fabricating fouling resistant nanocomposite membranes with high flux distillation. *Colloids Surf. A Physicochem. Eng. Asp.* **633**, 127858 (2022).
45. Shittu, T. & Altarawneh, M. Investigative properties of CeO₂ doped with niobium: A combined characterization and DFT studies. *Nanotechnol Rev* **11**, 191–203 (2021).
46. Sarif, M. et al. High-throughput synthesis of CeO₂ nanoparticles for transparent nanocomposites repelling *Pseudomonas aeruginosa* biofilms. *Sci. Rep.* **12**, 3935 (2022).
47. Shehata, N., Samir, E. & Kandas, I. Plasmonic-ceria nanoparticles as fluorescence intensity and lifetime quenching optical sensor. *Sensors (Switzerland)* **18**, 2818 (2018).
48. Shcherbakov, A. B. et al. CeO₂ nanoparticle-containing polymers for biomedical applications: A review. *Polymers* **13**, 924. <https://doi.org/10.3390/polym13060924> (2021).
49. Nosrati, H., Heydari, M. & Khodaei, M. Cerium oxide nanoparticles: Synthesis methods and applications in wound healing. *Mater. Today Bio.* **23**, 100823. <https://doi.org/10.1016/j.mtbio.2023.100823> (2023).
50. Fu, X. et al. Ceria nanoparticles: Biomedical applications and toxicity. *J. Zhejiang Univ.-Sci. B* **25**, 361–388 (2024).
51. Myshkina, A. V. et al. Optical and luminescent properties of ceria nanoparticles produced by gas phase method. *J. Phys. Conf. Ser.* **1461**, 012112 (2020).
52. Hudda, K., Rathee, B., Wati, M., Ranga, S. & Tyagi, R. Some applications of CeO₂ nanoparticles. *Orient. J. Chem.* **39**, 684 (2023).
53. Selvaraj, S. et al. Cerium oxide nanoparticles and their polymeric composites: Advancements in biomedical applications. *J. Inorg. Organomet. Polym. Mater.* **34**, 5691–5717 (2024).
54. Dhannia, T. *Structural and optical properties of polymer/ceria nanocomposites environmentally friendly synthesis of cerium nanoparticles for photocatalyst applications. View project.* <https://www.researchgate.net/publication/338571127>.
55. Morselli, D. et al. Ceria/gold nanoparticles in situ synthesized on polymeric membranes with enhanced photocatalytic and radical scavenging activity. *ACS Appl. Nano Mater.* **1**, 5601–5611 (2018).
56. Shehata, N., Meehan, K., Hudait, M. & Jain, N. Control of oxygen vacancies and Ce³⁺ concentrations in doped ceria nanoparticles via the selection of lanthanide element. *J. Nanoparticle Res.* **14**, 1 (2012).
57. Chakraborty, T. et al. Synthesis and optimization of ceria variants via sol-gel combustion method for environmental remediation. *Mater. Open Res.* **3**, 1 (2024).
58. Bugrov, A. N. et al. Hydrothermal synthesis of CeO₂ nanostructures and their electrochemical properties. *Nanosyst. Phys. Chem. Math.* **11**, 355 (2020).

59. Park, S. H. & Lee, D. C. A study of the electrical stability characteristics of a PVDF organic thin film fabricated by using the thermal vapor deposition method. *J. Korean Phys. Soc.* **35**, 4315 (1999).
60. Lei, T. et al. Electrospinning-induced preferred dipole orientation in PVDF fibers. *J. Mater. Sci.* **50**, 4342 (2015).
61. Makula, P., Pacia, M. & Macyk, W. How To correctly determine the band gap energy of modified semiconductor photocatalysts based on UV-Vis spectra. *J. Phys. Chem. Lett.* **9**, 6814–6817. <https://doi.org/10.1021/acs.jpcl.8b02892> (2018).
62. Tsunekawa, S., Fukuda, T. & Kasuya, A. Blue shift in ultraviolet absorption spectra of monodisperse CeO_{2-x} nanoparticles. *J. Appl. Phys.* **87**, 1318 (2000).
63. El Khalifi, M., Picaud, F. & Bizi, M. Electronic and optical properties of CeO₂ from first principles calculations. *Anal. Methods* **8**, 5045 (2016).
64. Khalifi, M. E., Picaud, F. & Bizi, M. Electronic and optical properties of CeO₂ from first principles calculations. *Anal. Methods* **8**, 5045–5052 (2016).
65. Zafirova, M. I., Myshkina, A. V. & Bazhukova, I. N. Producing and studying the optical properties of films based on cerium oxide nanoparticles. In *AIP Conference Proceedings* vol. 2313 (American Institute of Physics Inc., 2020).
66. Patsalas, P., Logothetidis, S., Sygellou, L. & Kennou, S. Structure-dependent electronic properties of nanocrystalline cerium oxide films. *Phys. Rev. B Condens. Matter Mater. Phys.* **68**, 035104 (2003).
67. Gaabour, L. H. Analysis of spectroscopic, optical and magnetic behaviour of PVDF/PMMA blend embedded by magnetite (Fe₃O₄) nanoparticles. *Opt. Photonics J.* **10**, 197–209 (2020).
68. Nandiyanto, A. B. D., Oktiani, R. & Ragadhita, R. How to read and interpret FTIR spectroscopy of organic material. *Indones. J. Sci. Technol.* **4**, 97–118 (2019).
69. Le, B. et al. Flexible piezoelectric PVDF/TPU nanofibrous membranes produced by solution blow spinning. *J. Mater. Res. Technol.* **24**, 5032 (2023).
70. Morali, A., Mandal, A., Skorobogatiy, M. & Bodkhe, S. Unleashing the piezoelectric potential of PVDF: A study on phase transformation from gamma (γ) to beta (β) phase through thermal contact poling. *RSC Adv.* **13**, 31234 (2023).
71. Shi, F., Ma, Y., Ma, J., Wang, P. & Sun, W. Preparation and characterization of PVDF/TiO₂ hybrid membranes with different dosage of nano-TiO₂. *J. Memb. Sci.* **389**, 522 (2012).
72. Mazloom, F., Masjedi-Arani, M., Ghiyasiyan-Arani, M. & Salavati-Niasari, M. Novel sodium dodecyl sulfate-assisted synthesis of Zn₃V₂O₈ nanostructures via a simple route. *J. Mol. Liq.* **214**, 46 (2016).
73. Safardoust-Hojjaghan, H., Salavati-Niasari, M., Amiri, O. & Hassanpour, M. Preparation of highly luminescent nitrogen doped graphene quantum dots and their application as a probe for detection of Staphylococcus aureus and E. coli. *J. Mol. Liq.* **241**, 1114 (2017).
74. Amiri, M., Pardakhti, A., Ahmadi-Zeidabadi, M., Akbari, A. & Salavati-Niasari, M. Magnetic nickel ferrite nanoparticles: Green synthesis by Urtica and therapeutic effect of frequency magnetic field on creating cytotoxic response in neural cell lines. *Colloids Surf. B Biointerfaces* **172**, 244 (2018).
75. Shaterian, M., Enhessari, M., Rabbani, D., Asghari, M. & Salavati-Niasari, M. Synthesis, characterization and photocatalytic activity of LaMnO₃ nanoparticles. *Appl. Surf. Sci.* **318**, 213–217 (2014).
76. Salavati-Niasari, M., Salemi, P. & Davar, F. Oxidation of cyclohexene with tert-butylhydroperoxide and hydrogen peroxide catalyzed by Cu(II), Ni(II), Co(II) and Mn(II) complexes of N,N'-bis-(α -methylsalicylidene)-2,2-dimethylpropane-1,3-diamine, supported on alumina. *J. Mol. Catal. A Chem.* **238**, 215 (2005).
77. Heydariyan, Z. et al. Facile preparation and characterization of SmMn₂O₅/Mn₂O₃/g-C₃N₄ nanocomposites for electrochemical hydrogen storage application. *Int. J. Hydrog. Energy* **90**, 1300–1312 (2024).
78. Monsef, R. & Salavati-Niasari, M. Tuning architectural synergy reactivity of nano-tin oxide on high storage reversible capacity retention of ammonium vanadate nanobelt array cathode for lithium-ion battery. *Mater. Sci. Eng. B* **310**, 117743 (2024).
79. Shehata, N. et al. Stretchable nanofibers of polyvinylidene fluoride (PVDF)/thermoplastic polyurethane (TPU) nanocomposite to support piezoelectric response via mechanical elasticity. *Sci. Rep.* **12**, 8335 (2022).
80. Sengupta, D. et al. Characterization of single polyvinylidene fluoride (PVDF) nanofiber for flow sensing applications. *AIP Adv.* **7**, (2017).
81. Carreau, P. J. & Vergnes, B. Rheological characterization of fiber suspensions and nanocomposites. In *Rheology of Non-Spherical Particle Suspensions* 19–58 (Elsevier, 2015). <https://doi.org/10.1016/B978-1-78548-036-2.50002-2>.
82. Mandal, A. & Nandi, A. K. Ionic liquid integrated multiwalled carbon nanotube in a poly(vinylidene fluoride) matrix: Formation of a piezoelectric β -polymorph with significant reinforcement and conductivity improvement. *ACS Appl. Mater. Interfaces* **5**, 747–760 (2013).
83. Garain, S. et al. Self-poled transparent and flexible UV light-emitting cerium complex-PVDF composite: A high-performance nanogenerator. *ACS Appl. Mater. Interfaces* **7**, 1298–1307 (2015).
84. Karan, S. K., Mandal, D. & Khatua, B. B. Self-powered flexible Fe-doped RGO/PVDF nanocomposite: An excellent material for a piezoelectric energy harvester. *Nanoscale* **7**, 10655–10666 (2015).
85. Liang, C. L. et al. Induced formation of dominating polar phases of poly(vinylidene fluoride): Positive ion-CF₂ Dipole or Negative Ion-CH₂ dipole interaction. *J. Phys. Chem. B* **118**, 9104–9111 (2014).
86. Gregorio, R. Determination of the α , β , and γ crystalline phases of poly(vinylidene fluoride) films prepared at different conditions. *J. Appl. Polym. Sci.* **100**, 3272 (2006).
87. Abdullah, I. Y., Jumali, M. H. H., Yahaya, M. & Shanshool, H. M. Facile formation of β poly (vinylidene fluoride) films using the short time annealing process. *Adv. Environ. Biol.* **9**, 20 (2015).
88. Muniz, F. T. L., Miranda, M. A. R., Dos Morilla Santos, C. & Sasaki, J. M. The Scherrer equation and the dynamical theory of X-ray diffraction. *Acta Crystallogr. A Found. Adv.* **72**, 385 (2016).
89. Viswanath, P. & Yoshimura, M. Light-induced reversible phase transition in polyvinylidene fluoride-based nanocomposites. *SN Appl. Sci.* **1**, 1519 (2019).
90. Shang, J., Liu, F., Gu, G. & Meng, L. Effects of Ce(NO₃)₃ concentration on microstructure and properties of plasma electrolytic oxidation layer on 6061 alloy. *Mater. Res. Express* **9**, 096513 (2022).
91. Riosbaas, M. T., Loh, K. J., O'Bryan, G. & Loyola, B. R. In situ phase change characterization of PVDF thin films using Raman spectroscopy. In: *Sensors and Smart Structures Technologies for Civil, Mechanical, and Aerospace Systems 2014* vol. 9061 (2014).
92. Chatterjee, A., Das, A., Saha, K. & Jeong, U. Nanofiller-induced enhancement of PVDF electroactivity for improved sensing performance. *Adv. Sens. Res.* **2**, 2200080 (2023).
93. Boccaccio, T., Bottino, A., Capannelli, G. & Piaggio, P. Characterization of PVDF membranes by vibrational spectroscopy. *J. Memb. Sci.* **210**, 315 (2002).
94. Constantino, C. J. L. et al. The investigation of $\alpha \rightarrow \beta$ phase transition in poly(vinylidene fluoride) (PVDF). In *Proceedings International Symposium on Electrets* vol. 2005 (2005).
95. Yurova, P. A., Tabachkova, N. Y., Stenina, I. A. & Yaroslavtsev, A. B. Properties of ceria nanoparticles with surface modified by acidic groups. *J. Nanoparticle Res.* **22**, 318 (2020).
96. Filtschew, A. & Hess, C. Interpretation of Raman spectra of oxide materials: The relevance of absorption effects. *J. Phys. Chem. C* **121**, 19280 (2017).
97. Kaspar, P. et al. Case study of polyvinylidene fluoride doping by carbon nanotubes. *Materials* **14**, 1428 (2021).
98. Saleh, S. M., Alminderej, F. M. & Mohamed, A. M. A. Superhydrophobic and corrosion behaviour of PVDF-CeO₂ composite coatings. *Materials* **15**, 8674 (2022).

99. Shlapa, Y. et al. Cerium dioxide nanoparticles synthesized via precipitation at constant pH: Synthesis, physical-chemical and antioxidant properties. *Colloids Surf. B Biointerfaces* **220**, 112960 (2022).
100. Ramasundaram, S., Yoon, S., Kim, K. J. & Park, C. Preferential formation of electroactive crystalline phases in poly(vinylidene fluoride)/organically modified silicate nanocomposites. *J. Polym. Sci. B Polym. Phys.* **46**, 2173–2187 (2008).
101. Martins, P. et al. Role of nanoparticle surface charge on the nucleation of the electroactive β -poly(vinylidene fluoride) nanocomposites for sensor and actuator applications. *J. Phys. Chem. C* **116**, 15790–15794 (2012).
102. Garain, S., Jana, S., Sinha, T. K. & Mandal, D. Design of in situ poled Ce³⁺-doped electrospun PVDF/graphene composite nanofibers for fabrication of nanopressure sensor and ultrasensitive acoustic nanogenerator. *ACS Appl. Mater Interfaces* **8**, 4532 (2016).
103. Rashid, M. H. *Power Electronics Handbook. Power Electronics Handbook* (2023). <https://doi.org/10.1016/C2021-0-02072-1>.
104. Ode, L., Hikam, M., Soegijono, B. & Sudarmaji, A. The electrical hysteresis loop and polarization value of BaZrxTi1-xO3 multilayer films material at different annealing temperature (x = 0.1 and 0.08) based on Sawyer Tower Circuit. In *Proceedings of the 2014 International Conference on Physics and its Applications* vol. 1 (2015).
105. Indolia, A. P. & Gaur, M. S. Optical properties of solution grown PVDF-ZnO nanocomposite thin films. *J. Polym. Res.* **20**, 1 (2013).
106. Elmezayyen, A. S., Zheng, J. & Xu, C. Simply preparation of self-poled PVDF/nanoceria nanocomposite through one-step formation approach. *Polym. Bull.* **78**, 5547–5566 (2021).
107. Li, H. et al. Enhancing the tactile and near-infrared sensing capabilities of electrospun PVDF nanofibers with the use of gold nanocages. *J. Mater. Chem. C Mater.* **6**, 10263 (2018).
108. Samadi, A., Hosseini, S. M. & Mohseni, M. Investigation of the electromagnetic microwaves absorption and piezoelectric properties of electrospun Fe₃O₄-GO/PVDF hybrid nanocomposites. *Org. Electron.* **59**, 149 (2018).

Acknowledgements

This research work has been funded by a research grant received by the British Embassy in Kuwait according to the project code (PUR 1035037). The open-access publication of this article was funded by the Priority Research Area SciMat under the program “Excellence Initiative – Research University” at the Jagiellonian University in Krakow. The study was carried out using research infrastructure funded by the European Union in the framework of the Smart Growth Operational Programme, Measure 4.2; Grant No. POIR.04.02.00-00-D001/20, “ATOMIN 2.0 – Center for materials research on ATOMIC scale for the INnovative economy”.

Author contributions

Nader Shehata: Conceptualization, Writing – Review and Editing, Methodology, Supervision, Project Administration and Funding Acquisition. Remya Nair: Writing Original Draft, Data Curation, Validation, Investigation and Formal Analysis. Ankur Jain: Writing – Review and Editing. Mohammed Gamal: Software and Formal Analysis. Ahmad Hassanin : Writing – Review and Editing. Sara Noman – Data Curation. Islam Shyha—Review and Editing. Krzysztof Kruczała-Methodology, Reviewing and Supervision, Marwa Saad- Methodology, Writing and Editing. Ishac Kandas : Writing, Supervision, Review and Editing, and Methodology.

Declarations

Competing interests

The authors declare no competing interests.

Additional information

Supplementary Information The online version contains supplementary material available at <https://doi.org/10.1038/s41598-025-98048-2>.

Correspondence and requests for materials should be addressed to M.S.

Reprints and permissions information is available at www.nature.com/reprints.

Publisher’s note Springer Nature remains neutral with regard to jurisdictional claims in published maps and institutional affiliations.

Open Access This article is licensed under a Creative Commons Attribution-NonCommercial-NoDerivatives 4.0 International License, which permits any non-commercial use, sharing, distribution and reproduction in any medium or format, as long as you give appropriate credit to the original author(s) and the source, provide a link to the Creative Commons licence, and indicate if you modified the licensed material. You do not have permission under this licence to share adapted material derived from this article or parts of it. The images or other third party material in this article are included in the article’s Creative Commons licence, unless indicated otherwise in a credit line to the material. If material is not included in the article’s Creative Commons licence and your intended use is not permitted by statutory regulation or exceeds the permitted use, you will need to obtain permission directly from the copyright holder. To view a copy of this licence, visit <http://creativecommons.org/licenses/by-nc-nd/4.0/>.

© The Author(s) 2025